CHALMERS
UNIVERSITY OF TECHNOLOGY

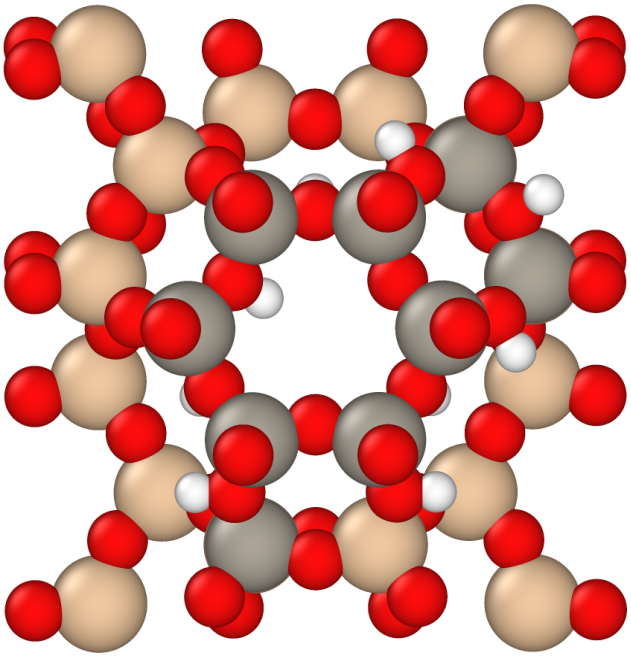

Chemical Ordering in Zeolites

A computational study of the aluminium distribution in SSZ-13

Master's thesis in Applied Physics

MAGNUS FANT

Department of Physics
CHALMERS UNIVERSITY OF TECHNOLOGY
Gothenburg, Sweden 2019

Master's thesis 2019:57124

Chemical Ordering in Zeolites

MAGNUS FANT

CHALMERS
UNIVERSITY OF TECHNOLOGY

Department of Physics
Materials and Surface theory
Computational Materials Group
Chalmers University of Technology
Gothenburg, Sweden 2019

Chemical Ordering in Zeolites
A computational study of the aluminium distribution in SSZ-13
MAGNUS FANT

Supervisor: Paul Erhart, Department of Physics
Examiner: Paul Erhart, Department of Physics

Master's Thesis 2019:57124
Department of Physics
Division of Surface and Materials Theory
Computational Materials Group
Chalmers University of Technology
SE-412 96 Gothenburg
Telephone +46 31 772 1000

Cover: Equilibrium configuration of Monte Carlo simulation with 9 Al at 600 K

Typeset in LaTeX
Printed by Chalmers Reproservice
Gothenburg, Sweden 2019

Chemical ordering in zeolites
A computational study of the aluminium distribution in SSZ-13
FANT MAGNUS
Department of Physics
Chalmers University of Technology

Abstract

Over the last century, zeolites have come to be among one of the most widely used catalysts. With their unique framework and ion exchanging capabilities zeolites show great promise for future applications in solar cells, water purification and thermal energy storage. Zeolites are a group of aluminosilicates, where the aluminium atoms is the origin to many of these interesting properties. In order be able to exploit the full potential of zeolites, more insight of regarding the aluminium distribution in the framework is required. By utilizing computational methods such as cluster expansions and thermodynamic Monte Carlo sampling, this thesis has shed some new light on how it is energetically favourable for Al to cluster in protonated SSZ-13. In addition, divalent counter ions was also examined and similar behaviour was found for them as well. These results prove that the generally accepted Löwenstein's rule does not apply for charge compensated zeolites.

Keywords: zeolites, SSZ-13, cluster expansion, DFT, MC, computational physics.

Acknowledgements

First off, I want to thank my supervisor and examiner Paul Erhart for all the help and guidance throughout this thesis. Without your intuition and vast knowledge in all matters related to materials- and computational physics this thesis would never have been possible. Secondly, I want to thank Mattias Ångqvist for your helpfulness and for your availabilty in exchanging thoughts and ideas for this thesis. I also want to express my gratitude towards the people in Materials and Surface Theory, especially Erik Fransson and Magnus Rahm. Lastly, I want to thank my family and friends for always being so supportive.

Magnus Fant, Gothenburg, June 2019

Contents

List of Figures

List of Tables

1
Introduction

Throughout the last 60 years zeolites have come to play a huge role in the field of catalysis. These porous materials had their breakthrough in the petrochemical industry in the early 1960s, paving the way for more efficient catalytic cracking and their ion exchange capabilities have found applications in detergents, adsorbents and in nuclear waste storage. They have also found usage in separation of gases.
What characterizes zeolites is their unique framework, and especially the cavities and tunnels that are present throughout the material. Zeolites are aluminosilicates, that consist of alumunium, silicon and oxygen. They are formed from tetrahedral building blocks, each of which contains four oxygen and either one silicon or one aluminium atom. The tetrahedra are linked together to form the zeolite structures. While theoretically, there is an infinite amount of zeolitic structures until now about 190 structures have been dicovered, either occuring naturally or created in synthetic ways [1].
The presence of aluminium atoms in the framework provides zeolites with properties that are sought after. A tetrahedron containing aluminium provides a negative net charge to the framework. To charge compensate, a counter ion enters the zeolitic network and neutralizes the negative contribution from the aluminium atoms. These counter ions can be exchanged easily, and together with voids and tunnels in the zeolite, give rise to the remarkable properties. By altering the amount of Al in the material, the catalytic properties of the zeolite can be fine tuned, as this changes both framework and charge.
Even though zeolites have been used heavily throughout the past half-decade, there is yet much to learn about this group of materials. For instance, little is known about how aluminium atoms are coordinated relative to each other. More insight in this field could open up for applications in various areas of technology. For instance, zeolites show great promise for usage in fuel cells, thermal energy storage, biomass conversion, water purification as well as CO_2 conversion [2].
The rapid development of computational power over the last decades has made computational physics an alternative to experimental methods. Through electronic structure calculations, one can acquire material quantities, such as energetics and band structures, of the material in question. These calculations, however, come at a rather high computational cost. Thus, they are not very well suited for studying chemical ordering in multi-component systems because to be able to draw any realistic conclusions an adequate sampling of the configuration space is required. A more suitable approach for ordering phenomena is by cluster expansions, which allow for comprehensive sampling of the chemical configuration space while being both accurate and computationally efficient. In combination with Monte Carlo sim-

ulations the cluster expansions can be employed to study various thermodynamical properties of the scrutinized material.
The aim of this thesis was to further investigate the distribution of aluminium in zeolites, more specifically the chabasite SSZ-13. This was done using different computational techniques. These techniques include empirical potentials, density functional theory calculations, cluster expansions and Monte Carlo simulations. Cluster expansions were succesfully used to describe the underlying energetics of this group of materials.

2
Theory

In this chapter the theory needed for this thesis is presented. This includes general background on zeolites, their formation and characteristics. The computational methods that have been used in this thesis are also presented along with the underlying theory.

2.1 Zeolites

Zeolites are aluminosilicate minerals, which come in various forms and shapes. They mainly consist of aluminium and silicon units, more specifically of tetrahedral building blocks of SiO_4 and AlO_4. These tetrahedra bind to each other via common oxygen atoms, and are commonly referred to as T-sites. It should be noted that T-sites can be occupied by other metals as well, such as iron and titanium [3]. They are often referenced as the primary building unit of zeolites. Due to the valency of Si atoms, they tend to form bonds in this tetrahedral manner. In the case of the tetrahedra in zeolites, the binding with Si results in a negative net charge of two electrons. Tetrahedra share two common O atoms with one another, which results in zero charge [4]. The building blocks that contain Al, however, will contribute a negative charge, since they have one valence electron less than Si. Examples of these tetrahedra are shown in Figure 2.1.

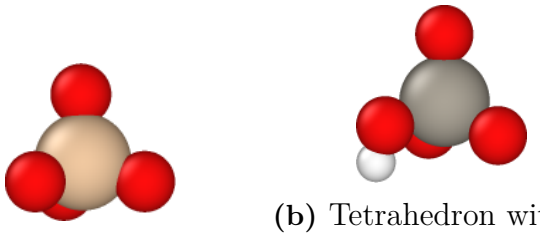

(a) Tetrahedron with Si

(b) Tetrahedron with Al and compensating proton

Figure 2.1: The form of the tetrahedron that act as the building block in the zeolitic framework. Observe that in 2.1b the Al atom has been charge compensated with a proton.

These tetrahedral elementary blocks give rise to complex structures and forms. The secondary building units in zeolites, which consists of tetrahedra put together, can take various forms and shapes. Channels and pores are formed throughout the lattice of the zeolite. These voids are actually one of the features that render zeolites such

an interesting group of materials, as they determine what kind of molecules can enter the framework, acting as a molecular sieve [5]. The secondary building units come in a variety of shapes, including rings, squares and hexagon as well ascubes and hexagonal prisms [6]. These are only a few examples of the different secondary building blocks, and they can, theoretically, be combined together in infinitely many ways.

2.1.1 Aluminium distribution of zeolites

Our understanding is incomplete concerning how aluminium atoms are distributed relative to each other in the zeolitic frameworks. The basic structure of the zeolitic framework can be determined by X-ray diffraction. Although a lot of the information concerning chemical composition and the framework of the zeolite can be obtained in this manner, the aluminium distribution in the system cannot be established. This is due the almost identical behaviour of Si and Al under X-ray spectroscopy, making them almost impossible to distinguish [7], and the correlations of sites cannot be provided by diffraction techniques. During synthesis, the Si/Al ratio can be tailored to the intended application, but little is known about how the aluminium atoms actually occupy the structure [8]. Since the aluminium atoms are the source of the sought-after properties, much research has been put into this. The most commonly cited rule that exists within the field of Al occupation in zeolites is Löwenstein's rule, which states that two aluminium atoms cannot share the same oxygen atom in their tetrahedra. Altough there are no experimental evidence of this rule, it is frequently invoked to rationalize data, even of the computational kind [9]. There is, however, studies that show that this rule does not always apply [10].

2.1.2 Binding sites of counter ions

The charge compensation of Al atoms in the zeolites occurs during synthesis. Depending on synthesis conditions, and what reactants are used, the counter ion species differ. Due to the ion exchange properties of zeolites, the counter ions can be swapped for other species afterwards. The species of the counter ion is crucial for the catalytic and adsorbing properties of the zeolite, so depending on application different cations are used. The counter ions is usually part of the alkali, alkaline earth and transition metals such as Na^+, Li^+, Mg^{2+}, Ca^{2+} and Cu^{2+} [11] [12]. An important special case of a counter ion is the proton, which gives rise to many of the acidic catalytic properties in zeolites [13]. The binding sites for the ions depends on their size and valency. Studies have shown that protons tend to be associated with an oxygen linked to the Al tetrahedra, while other monovalent cations such as Na^+ occupy interstitial sites [10]. Divalent counter ion species, like $Cu_2{}^+$, is also sited interstitailly between O atoms [14].

2.2 Statistical dynamics and computational methods

When looking at the behaviour of systems of particles, statistical mechanics provides a powerful mathematical framework for finding relations between microscopic phenomena of individual particles to macroscopic quantities. Thus, it relates thermodynamical concepts to quantum mechanics, or other theories of physics. In this thesis, statistical physics plays a major role in the computational methods that was used. The main concept that arises from this are thermodynamical ensembles, which can be explained from a statistical viewpoint and considered computationally through molecular dynamics and Monte Carlo integration. In this section, these concepts are introduced and explained.

2.2.1 The canonical ensemble

By considering a system in contact with a thermal resorvoir, we obtain the canonical ensemble. The canonical ensemble is characterized by a fixed temperature, but where energy can be exchanged between the system and the resorvoir. The system can thus be described with fixed (N, V, T). The energy can is expressed as $E_0 = E + E_r$, where E and E_r is the energy of the system and the reservoir respectively. This means that the full energy is constant, but that the internal energy of the system varies. In this part we want to derive the partition functions of the canonical ensemble, since it contains all of the thermodynamic properties of such a system.
To describe the macrostate of the full sytem we have to consider the microstates of both the resorvoir, Ω_r, and the system of particles Ω_s. By putting the total number of microstates in Boltzmann's formula we get

$$S = k_{\mathrm{B}} \ln \Omega_s \Omega_r = S_s + k_{\mathrm{B}} \ln \Omega_r \tag{2.1}$$

using the logarithmic rule. We now denote that the microstates depend on the energy so the second term in (2.1) can be expanded around E_0 as

$$\ln \Omega(E_0 - E) \approx \ln \Omega_r(E_0) + \left(\frac{\partial \ln \Omega_r}{\partial E_0}\right)(E_r - E). \tag{2.2}$$

By using the definition of temperature, i.e.

$$\frac{1}{T} = \left(\frac{\partial S}{\partial E}\right)_{N,V} \tag{2.3}$$

we insert this into the expansion in (2.2) and get the following expression for the full entropy of the system

$$S_{tot} = S_s - \frac{E}{T} + k_{\mathrm{B}} \ln \Omega_r(E_0). \tag{2.4}$$

When it comes to ordering of materials, not only does the entropy play a role, but also the energy. This is expressed in the Helmholtz free energy

$$F = U - TS, \tag{2.5}$$

where U is the internal energy of the system. The partition function for the canonical ensemble stems from taking every microstate into consideration. As a consequence of Eq. (2.4) the probability of finding the system in a certain microstate is

$$P = C \exp\Big(- \frac{E}{k_{\mathrm{B}} T}\Big), \tag{2.6}$$

where C is a constant. Due the fact that a summation over all microstates sums up to 1, $C = \sum_s \exp(-\beta E)$ where $\beta = 1/k_{\mathrm{B}}T$. This sum is also known as the partition function and is related to the Helmholtz free energy as

$$\mathcal{Z} = \exp(-F\beta). \tag{2.7}$$

This function contains all of the proper thermodynamical information to describe the system, but the problem lies within computing it for each possible microstate [15].

2.2.2 Molecular dynamics

Molecular dynamic simulations are based on Newton's equation of motion. They are performed by choosing an initial configuration of the system, defining an interatomic potential and then letting the system evolve in time through the usage of algorithms like Verlet integration. The simplest type of a molecular dynamic simulation samples the microcanonical ensemble, since it conserves the energy. Other ensembles can be represented by adding thermostats and/or barostats. The acquired results from this kind of simulation are obtained time-averaging, as the microstates evolve over time. This kind of measurements can be mathematically expressed as

$$\bar{f} = \lim_{t\to\infty} \frac{1}{t} \int_0^t \mathrm{d}t' f(\boldsymbol{r}(t'), \boldsymbol{p}(t')), \tag{2.8}$$

which simply means averaging some quantity f over time where $\boldsymbol{r}$ and $\boldsymbol{p}$ denote positions and momenta, respectively.

2.2.3 Monte Carlo integration

The essence of Monte Carlo (MC) algorithms is the usage of random numbers to sample multidimensional integrals. Unlike molecular dynamic simulations, MC integration for physical properties relies on averaging over phase space instead of over a time interval. To this end, the density function for the ensemble has to be known as it acts as the distribution function for the system. Such a measurement can be expressed as

$$\Big\langle f \Big\rangle = \frac{\int \mathrm{d}\boldsymbol{r}\mathrm{d}\boldsymbol{p} f(\boldsymbol{r},\boldsymbol{p})\rho(\boldsymbol{r},\boldsymbol{p})}{\int \mathrm{d}\boldsymbol{r}\mathrm{d}\boldsymbol{p}\rho(\boldsymbol{r},\boldsymbol{p})}, \tag{2.9}$$

where f is the measured variable and ρ is the density of the system. The ergodic hypothesis, which states equality between (2.8) and (2.9)

$$\bar{f} = \Big\langle f \Big\rangle \tag{2.10}$$

is often used in the field of computational physics.
There are multiple ways of carrying out MC integration, with the most simple one being sampling on a uniform interval. There are, however, ways to make the sampling more accurate and efficient. This can be accomplished through importance sampling. This means that a probability density $\rho(x)$ is introduced, which will guide the random walk through phase space to configurations that are more probable. This is done by carrying out a trial step, evaluating the ratio of $\rho(x)$ for the trial state and the current state, and depending on the outcome the step is accepted or rejected [16]. The most common method for this is the Metropolis algorithm [17]. A trial step for such a routine can be described by

$$P = \min\{1, \rho(\text{trial})/\rho(\text{current})\}, \tag{2.11}$$

where P is the probability of accepting a step.

2.3 Density functional theory

Density functional theory (abbreviated DFT) is one of the most widespread techniques within computational physics. It is based on the fact that every property of a material can be described by the ground state electron density. The theory behind DFT is remarkably simple as formulated in the Hohenberg-Kohn theorems. These theorems do not, however, provide a way of employing DFT to any real applications. Kohn and Sham provided an ansatz paving the way to calculating properties of many-electron systems. The theorems, derivations and conventions used here follows the presentation by R. Martin [18].

2.3.1 Hohenberg-Kohn theorems

The theorems declared by Hohenberg and Kohn provides a way for finding the ground state density of the electrons in a many particle problem. The Hamiltonian for such a many particle system can be written as

$$\hat{H} = -\frac{\hbar^2}{2m_e}\sum_i \nabla_i^2 + \sum_i V_{\text{ext}}(\mathbf{r}) + \frac{1}{2}\sum_{i\neq j}\frac{e^2}{|\mathbf{r}_i - \mathbf{r}_j|}, \tag{2.12}$$

where the first term of this equation describes the kinetic energy, the second is the contribution of a external potential and the last term is the interaction between electrons.
Theorem 1 *The external potential V_{ext} working on a system of interacting particles is determined uniquely by the ground state density of the particles $n_0(\boldsymbol{r})$.*
This theroem is proved by considering two external potentials which differ from each other by more than a constant and which lead to the exact same ground state energy. This means that the Hamiltonians, $\hat{H}^{(1)}$ and $\hat{H}^{(2)}$, for the systems will differ, as well as the ground state wavefunctions $\Psi^{(1)}$ and $\Psi^{(2)}$. By using that $\Psi^{(2)}$ does not correspond to the ground state of $H^{(1)}$ the following equality can be written

$$E^{(1)} = \left\langle \Psi^{(1)} \middle| \hat{H}^{(1)} \middle| \Psi^{(1)} \right\rangle < \left\langle \Psi^{(2)} \middle| \hat{H}^{(1)} \middle| \Psi^{(2)} \right\rangle, \tag{2.13}$$

under the assumption that the ground state is non-degenerate. By rewriting the last term in (2.13) and using the Hamiltonian from (2.12) the following expression is acquired

$$\left\langle \Psi^{(2)} \right| \hat{H}^{(1)} \left| \Psi^{(2)} \right\rangle = \left\langle \Psi^{(2)} \right| \hat{H}^{(2)} \left| \Psi^{(2)} \right\rangle - \left\langle \Psi^{(2)} \right| \hat{H}^{(1)} - \hat{H}^{(2)} \left| \Psi^{(2)} \right\rangle \tag{2.14}$$

$$= E^{(2)} + \int \mathrm{d}^3 r \Big[V_{\mathrm{ext}}^{(1)} - V_{\mathrm{ext}}^{(2)} \Big] n_0(\mathbf{r}). \tag{2.15}$$

The inequality can thus be written as

$$E^{(1)} < E^{(2)} + \int \mathrm{d}^3 r \Big[V_{\mathrm{ext}}^{(1)} - V_{\mathrm{ext}}^{(2)} \Big] n_0(\mathbf{r}). \tag{2.16}$$

By using the same procedure for $E^{(2)}$ we find that

$$E^{(2)} < E^{(1)} + \int \mathrm{d}^3 r \Big[V_{\mathrm{ext}}^{(2)} - V_{\mathrm{ext}}^{(1)} \Big] n_0(\mathbf{r}). \tag{2.17}$$

If the two inequalities in Eq. (2.16) and Eq. (2.17) are added the resulting inequality reads $E^{(1)} + E^{(2)} < E^{(1)} + E^{(2)}$, which is contradictory. This also proves the theorem; a non-degenerate electron density cannot be identical for two external potentials that differ by more than a constant. The potential is, however, uniquely determined by the electron density to within a constant. A corollary to this theorem is that since the Hamiltonian is uniquely determined by the ground state density but for a constant shift in the energy, the many-body wavefunctions for all states are determined.

Theorem 2 *Independent of the external potential V_{ext}, a universal functional for energy $E[n]$ can be defined. The ground state energy of the system will be the global minimum value of this functional, and the density $n(\boldsymbol{r})$ corresponding to this value will be the ground state density of the system, for any external potential V_{ext}.*

This theorem is proved by considering the fact that all properties of a system are determined by the electron density $n(\mathbf{r})$. These properties can be seen as a functional of $n(\mathbf{r})$. The total energy functional for such a system is described as

$$E_{\mathrm{HK}} = T[n] + E_{\mathrm{int}}[n] + \int \mathrm{d}^3 r V_{\mathrm{ext}}(\mathbf{r}) n(\mathbf{r}) + E_{II}, \tag{2.18}$$

where the first two terms corresponds to the kinetic and potential energies respectively, the third term to the contribution from the external potential and the last term is the interaction energy of the nuclei. In addition, the first two terms must be universal since they only depend on the density.

Consider two different densities $n^{(1)}(\mathbf{r})$ and $n^{(2)}(\mathbf{r})$. The external potential $V_{\mathrm{ext}}^{(1)}$ corresponds to $n^{(1)}$, and the expectation value of the Hamiltonian in the ground state with wavefunction $\Psi^{(1)}$ is

$$E^{(1)} = E_{\mathrm{HK}}[n^{(1)}] = \left\langle \Psi^{(1)} \right| \hat{H}^{(1)} \left| \Psi^{(1)} \right\rangle. \tag{2.19}$$

Naturally, the other density $n^{(2)}$ with $\Psi^{(2)}$ has a higher energy for the same external potential i.e.

$$E^{(1)} = \left\langle \Psi^{(1)} \right| \hat{H}^{(1)} \left| \Psi^{(1)} \right\rangle < \left\langle \Psi^{(2)} \right| \hat{H}^{(1)} \left| \Psi^{(2)} \right\rangle = E^{(2)}. \tag{2.20}$$

This means that the energy in terms of the Hohenberg-Kohn functional for the correct ground state density $n_0(\mathbf{r})$ is lower than for any other density $n(\mathbf{r})$. A corollary to this theroem is that if the part of the functional describing the internal energies

$$F_{\mathrm{HK}} = T[n] + E_{\mathrm{int}}[n] \tag{2.21}$$

is known then the exact ground state density can be obtained by minimizing the total energy of the system. By using the two theorems, a self-consistency loop can be defined for finding the ground state density of the system. This loop can be seen in Figure 2.2. The should be noted that these theorems do not provide any practical way of solving the many-body wavefunctions.

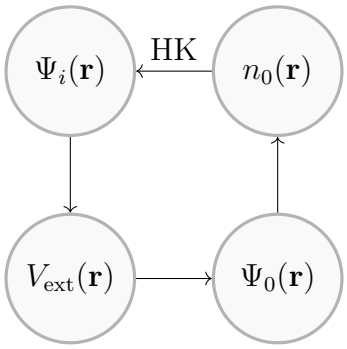

Figure 2.2: By utlizing the Hohenberg-Kohn theorems, the ground state density of the observed system can be determined iteratively through this procedure.

2.3.2 DFT in practice: The Kohn-Sham equation

Although the Hohenberg-Kohn theorems provide an exact theory, they do not grant real means to solve the equations for many-particle systems. The difficulty lies in the interactions between the particles in such a system. The Kohn-Sham approach is to replace the interacting system with an auxiliary one that still incorporates all the dynamics of the interacting one. To be able to do this, they made an ansatz based on two assumption; firstly, the ground state density for the non-interacting system is the same as for the interacting one. Secondly, it is assumed that the the auxiliary Hamiltionian contains the usual operator for the kinetic part of the energy but and effective local potential $V_{\mathrm{eff}}^{\sigma}(\mathbf{r})$. The energy functional for such a system is

$$E_{\mathrm{KS}} = T_s[n] + \int \mathrm{d}\mathbf{r} V_{\mathrm{ext}}(\mathbf{r}) n(\mathbf{r}) + E_{Hartree}[n] + E_{\mathrm{xc}}[n]. \tag{2.22}$$

This representation is quite similar to that of the Hohenberg-Kohn functional in Eq. (2.18), but with some modifications. The first term in Eq.(2.22) is due to the kinetic energy of the system, the second term rises from the potential of the nuclei and other external fields, the third is the Hartree term which stems from the Coulomb interaction energy and the fifth term represents the nucleic interactions and the last one is due to exchange-correlation. The ingenuity in the ansatz lies in separating the independent kinetic energies of the particles as well as the long range interactions in the Hartree terms, which means that the exchange-correlation term

can be approximated as a local functional. The form of the exchange-correlation functional can be written as

$$E_{\mathrm{xc}}[n] = \frac{1}{2}\int \mathrm{d}^3 r n(\mathbf{r}) \int \mathrm{d}^3 r' \frac{\bar{n}_{\mathrm{xc}}(\mathbf{r}, \mathbf{r}')}{|\mathbf{r} - \mathbf{r}'|}. \tag{2.23}$$

The $\bar{n}_{\mathrm{xc}}$ represents the exchange-correlation hole, and there is no exact solution to how this actually looks. When it comes to the accuracy of actual DFT calculations the choice of exchange-correlation functional is key for the success of the calculations. The Kohn-Sham ansatz provide a way to use DFT in practice. As Hohenberg and Kohn provided a self-consistency loop for iteratively finding the electron density of the ground state of an interacting many-body system, the ansatz proposed by Kohn and Sham provides a way of using DFT in practice. The self-consistency loop complemented with the ansatz is shown in figure 2.3.

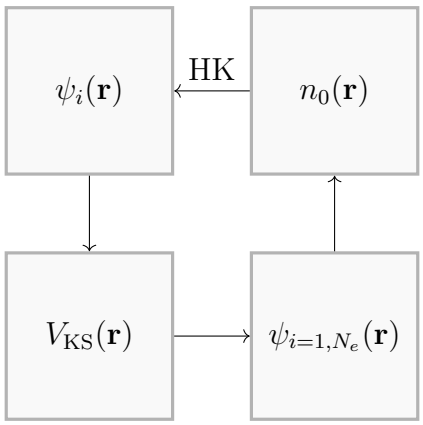

Figure 2.3: The Kohn-Sahm ansatz provides a way of finding the ground state properties of a many-body system self-consistently.

2.4 Cluster expansions

While density functional theory is a great tool for acquiring different properties of materials, is comes with a high computational cost. In many, cases this is not a major drawback, but when the chemical ordering in a material is of interest, alloy cluster expansions provide a more efficient way to acquire the wanted property. This is done by looking at a variation of a property for different configurations of the chemical compounds in the lattice. In this section, the theory behind cluster expansions is presented.

2.4.1 Clusters

A cluster expansion is performed by decomposing the structure into clusters. Since the clusters are parts of the underlying lattice, they are affected by its symmetry. Cluster can be transformed into each other by the use of symmetric operations. Clusters that transforms into each other under these operations belong to the same orbit. An orbit is represented by a symmetry inequivalent cluster that can be transformed

into any cluster which belongs to the orbit [19]. It is customary to describe clusters in orders of singlet, pairs, triplets, quadruplets etc. The cluster size is defined as the average distance to the lattice points from the geometric center of the cluster. Due to the short-ranged nature of physical interactions clusters of higher orders contribute less. In addition, this also limits the size of the cluster, since interactions between largely separated atoms will be small and thus can be neglected.

2.4.2 Constructing the cluster expansion

By constructing a complete orthogonal basis a CE can represent any function of the configuration $Q(\boldsymbol{\sigma})$, where $\boldsymbol{\sigma}$ is the occupation vector. For a binary system, the occupation vector consists of 0 and 1 depending on what species occupy the lattice point. For each lattice site p one can define M orthogonal point functions

$$\Theta_n(\sigma_p) = \begin{cases} 1, & \text{if } n = 0 \\ -\cos(\pi(n+1)\sigma_p/M), & \text{if } n \text{ is odd} \\ -\sin(\pi n\sigma_p/M), & \text{if } n \text{ is even} \end{cases}, \tag{2.24}$$

where M is the allowed number of species and n is the point function index, which goes from $n = 0, 1, ...M-1$ [20].
These point functions can be used to form a complete orthogonal set of functions $\Pi_\alpha(\boldsymbol{\sigma})$ in configuration space as

$$\Pi_\alpha^{(s)}(\boldsymbol{\sigma}) = \Theta_{n_1}(\sigma_1)\Theta_{n_2}(\sigma_2)...\Theta_{n_l}(\sigma_\alpha), \tag{2.25}$$

where l defines the number of sites in the cluster and α corresponds to the set of point function indices n_i. Due to the completeness and orthogonality of the basis set they can be used to form any function of the configuration and all basis function Π have one configuration invariant component for the case $\boldsymbol{\alpha} = 0$, so that any function of the configuration can be expressed as

$$Q(\boldsymbol{\sigma}) = Q_0 + \sum_\alpha \sum_s \left\langle \Pi_{\alpha'}^{(s)}(\boldsymbol{\sigma}) \right\rangle_\alpha m_\alpha^{(s)} J_\alpha^{(s)}. \tag{2.26}$$

Q_0 denotes the configuration invariant term, m_α is the multiplicity of the representative cluster α and J_α are the effective cluster interactions (ECIs), which are the free parameter that render a cluster expansion. When constructing a CE the ECIs must be determined. To this end reference data for a set of configurations $\boldsymbol{\sigma}_1, \boldsymbol{\sigma}_2, ..., \boldsymbol{\sigma}_n$ is needed, as well as a vector of target data Q^T. The full expression for the configuration in Eq. (2.26) can be rewritten as

$$\boldsymbol{Q} = \boldsymbol{\Pi J}. \tag{2.27}$$

Here, the rows of $\boldsymbol{\Pi}$ are given by

$$\boldsymbol{\Pi}_i = [1, \left\langle \Pi_{\boldsymbol{\alpha}_1'}(\boldsymbol{\sigma}_i) \right\rangle_{\boldsymbol{\alpha}_1} m_{\boldsymbol{\alpha}_1}, \left\langle \Pi_{\boldsymbol{\alpha}_2'}(\boldsymbol{\sigma}_i) \right\rangle_{\boldsymbol{\alpha}_2} m_{\boldsymbol{\alpha}_2}, ...]$$

and $\boldsymbol{J}$ represents the ECIs with $J_0 = Q_0$. In reality, obtaining the ECIs is done by solving eq. (2.27), which is a linear system. Often, the system is underdetermined

and the rows the sensing matrix Π are correlated. Also, due to the short range of the physical interactions the solution for the ECIs can be sparse. This can be obtained numerically by feature selection, which is able to yield models that are less prone to overfitting, have a greater transferability and even reduce the computational cost of the procedure. To this end, a variety of optimizng techniques can be used. The ones used in this thesis are the least absolute shrinkage and selection operator (LASSO), recursive feature elimination (RFE) and automatic relevence detection regression (ARDR), which is a Bayesian linear regression technique.
To compare the performance of different models cross-validation (CV) is used. This is done by splitting the reference data into training and validation sets. The former is used for obtaining the ECIs and the latter is later used as a reference when looking at the root mean squared error (RMSE) of the acquired CE as

$$\mathrm{RMSE} = \sqrt{\frac{1}{N_s}\sum_i (Q_i^{\mathrm{model}} - Q_i^{\mathrm{target}})}, \tag{2.28}$$

where N_s is the number of structures in the validation set [21].

3

Methodology

The methodology used throughout the project is presented in this chapter. During the study a variety of methods was used, both for purposes of validating the procedure as well as validating the results obtained by their usage. Examples include the comparison between different exchange-correlation functionals for the relaxation of the structures, optimizations methods used in the training of the cluster expansions as well as trying out empirical potentials and DFT for the relaxation of the structures. Generally, for the cluster expansions, the standard procedure for this type of computations were used. A flowchart of the subroutines used for creating and employing cluster expansions can be seen in Figure 3.1.

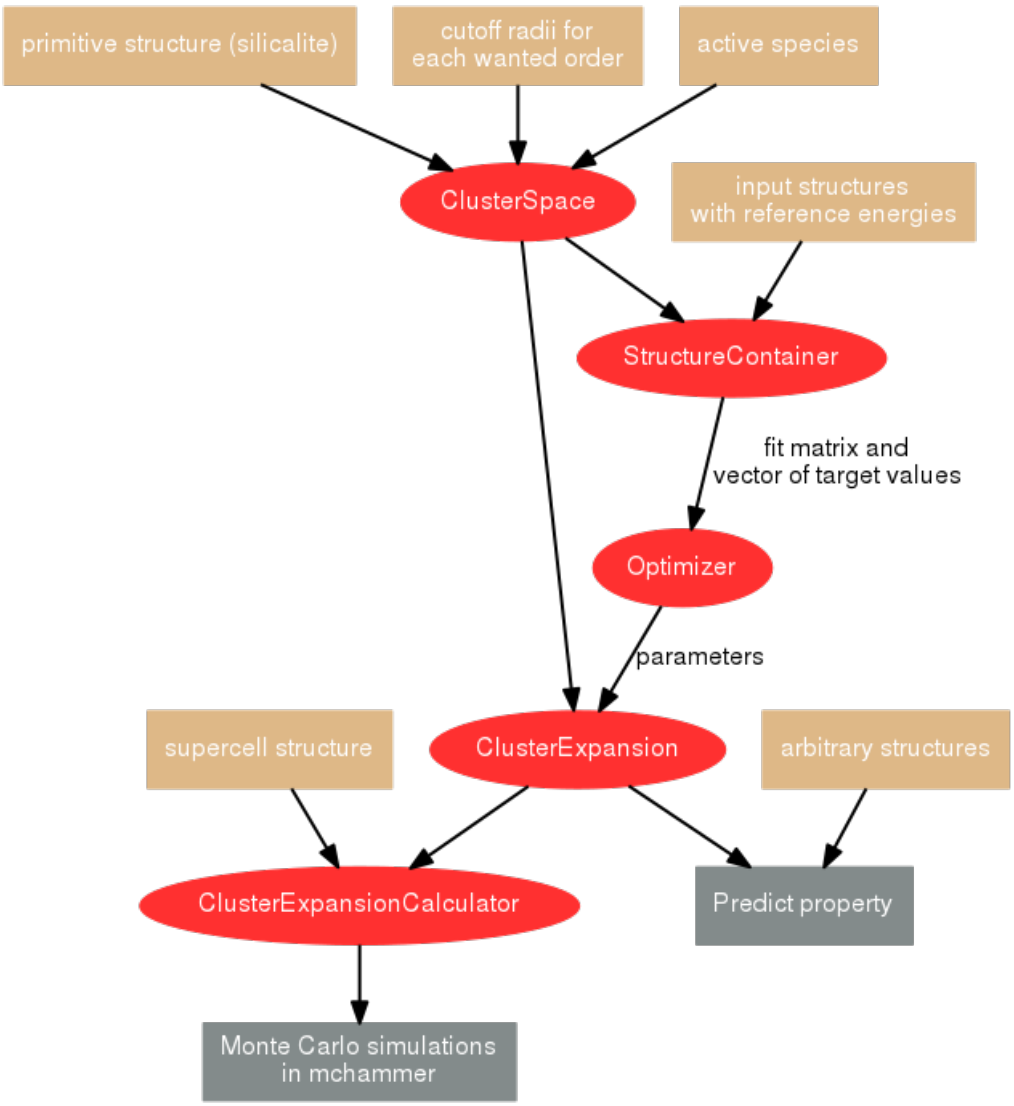

Figure 3.1: The general workflow for constructing and employing cluster expansions.

3.1 Structure generation

Most of the structures generated for this work was done using the enumeration routine in ICET [21], whereas format conversions and data handling were carried out using the Atomic Simulation Environment (ASE) [22]. Structures were generated from the primitive uni cell, which only included T-sites containing Si. The primitive structure was retrieved from the *Database of Zeolite Structures*, which is a database created by the International Zeolite Association [23]. The primitive unit cell can be seen in Figure 3.2a.

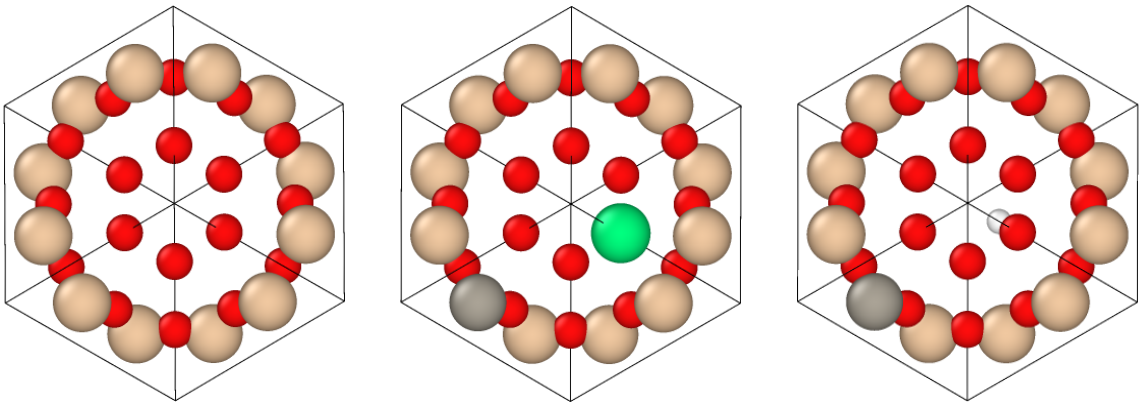

(a) Primitive unit cell **(b)** Enumerated OH site **(c)** OH exchanged for H

Figure 3.2: (a) Primitive unit cell of SSZ-13. It contains 12 T-sites (beige), and 24 oxygen sites (red) with a total of 36 atoms in the pure Si form (silicalite). (b) One of the enumerated structures is shown, obtained by enumerating both Al over the T-sites and all of the possible O sites. (c) shows the same configuration right before relaxation. The atom representing the OH group is exhanged for for an oxygen atom and an appended hydrogen.

When generating structures, three different procedures were used. The first way of constructing reference structures consisted of randomly distributing out Al atoms over the T-sites in the unit cell. This kind of random distribution was mainly used in attempts to create structures comprising more than the unit cell. Because of the high number of possible T-sites in supercells, enumeration of them would be tedious and the amount of possible configurations rises rapidly with the number of sites in the structure. The enumeration scheme works in the manner that it finds every unique possible configuration given the symmetry of the structure. In the case of the chabasite used throughout this thesis, there are 12 T-sites in the primitive unit cell. For this primitive unit cell, there are one unique way of replacing a single Si atom with Al, 9 ways of distributing out two Al atoms and 19 ways of distributing 3 Al atoms in the structure. This follows the rules of combinatorics and the number of configurations increases rapidly with an increasing number of Al T-sites.

3.1.1 Binding sites of counter ions

Depending on what counter ion was used in the calculations, different methodologies were used. In the case of protons as counter ions, three different methods in distributing the proton were considered. Divalent counter ions were allowed to occupy two different sites in the primitive unit cell of SSZ-13, where the positions were taken from the work of Fickel and Lobo [14].

3.1.1.1 Protons as counter ions

Initially in the project, each aluminium was charge compensated by placing the hydrogen at one of the four O atoms that are part of the tetrahedron. A cost function was used to get the optimal position for the hydrogen.

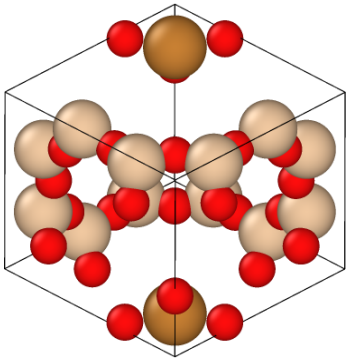

Figure 3.3: The binding sites for the divalent counter ions in the pure silicalite. The binding sites are represented by the large, rust colored atoms.

During the work the binding sites of the protons species were also investigated. To generate the structures relevant for these type of calculations in the case of protons, a double enumeration routine was used. No assumptions for the hydrogenic binding sites were made, instead distributing the charge compensating protons in the same manner as for the Al atoms in the simple enumeration scheme. In practice, the enumeration was done using one atom representing the OH that is formed. This means that the sublattice of possible O sites was enumerated with the same concentration of OH as that of Al in the system.

The amount of structures rises rapidly with the concentration of Al, with 24 unique ways of distributing one Al and a charge compensating proton. An example for such a structure can be seen in Figure 3.2b. In the case of the double enumeration scheme, the OH species, has to be changed to an O with an appended proton before relaxation. This is shown in Figure 3.2c.

3.1.1.2 Divalent counter ions

The placement of the divalent counter ion sites can be seen in Figure 3.3. Since there are only two possible sites for this type of counter ions, it also constrains the number of Al atoms to two or four in the primitive unit cell. Since this restricts the number of possible configurations, the enumeration scheme were run for all primitive unit cell structures and the possible sites for supercells twice the size of the primitive unit cell. The divalent species used in this thesis were Mg, Ca, Se, Ba, Cu, and Zi.

3.2 Relaxation of structures

To obtain the ground state energy of a structure it needs to be releaxed. This was mainly performed in two different manners: by using the empirical reactive force field [24] as implemented in the LAMMPS (Large-scale Atomic/Molecular Massively Parallel Simulator) software [25] and DFT calculations using the Vienna Ab initio Simulation Package (VASP) [26] [27].

3.2.1 Force field calculations

The reactive force field used here was developed specifically for modelling the usage of methanol to olefin reactions in the ZSM-5 zeolite [24]. This method was only used in the beginning of the thesis work, in order to see if the low computational cost of empirical potentials would outweigh the DFT based relaxations, since the latter are associated with a much higher computational cost.

3.2.2 DFT calculations

The DFT calculations done in this thesis mainly followed the same setup. Three different exchange-correlation functionals were used in order to validate the result of the calculations. The other parameters, however, were kept identical for all of the relaxations. As convergence criteria, the maximal forces acting on the system was set to have a threshold of 25×10^{-3} eV/Å and the energy difference between ionic relaxation steps were set to 10^{-5} eV. When both of these criteria were reached, the structure was considered releaxed. The plane wave energy cutoff for the calculations was set to 520 eV. Since cell relaxation was of interest, not only the positions were allowed to relax but also cell volume and shape. As for the minimization algorithm used, most of the relaxations started by using the conjugate-gradient method to get close to the global minimum of the energy, and then switched to using the quasi-Newton algorithm, which performs better close to the minimum but worse in the initial steps of the relaxation.
All of the three functionals used throughout the project were of the generalized gradient approximation (GGA) kind, which considers the gradient of the density unlike the more simple local density approximation (LDA) functional [28]. Initially in the project, the vdW-DF-cx functional was used [29]. This functional takes van-der-Waals contributions into account, which can be necessary when describing systems where covalent and electrostatic bonds are important and acts as a GGA functional but with a non-local correction term which includes the van-der-Waals contributions [29]. These calculations were validated using two other functionals, namely PBE and PBEsol. PBE is one of the most common functionals in the field of DFT, because of its generality [30]. The PBEsol is a revision of the PBE functional, where the equilibrium properties of dense solids are more accurate than for its predecessor [31]. After the validation of the functionals, PBE was chosen for the remainder of the project since it yields very similar results as the other two functionals while it is substantially easier to use in terms of the relaxation behaviour.

3.3 Cluster expansions

When creating a cluster expansion, the workflow followed the order in Figure 3.1. Below follows a more detailed description of the construction of the cluster expansion, what parameters were taken into account and how the expansions were sampled.

1. When setting up the cluster space for the cluster expansion a primitive unit cell with only Si occupying the T-sites was used. This is referred to as the silicalite

in Figure 3.1. The active species were also set up, which differed depending on the counter ion species. When enumerating both the T-sites and the ionic bonding sites, two active sublattices were used. To find appropriate cutoff and expansion orders, different combinations of these parameters were compared using the cross-valkidated RMSE. By setting cutoffs, the expansion order, the active species and the ideal lattice a representation of the SSZ-13 structure is dcomposed in terms of cluster vectors. A cluster vector is a way of numerically describing a structure of mixed species.

2. After the cluster space had been constructed, a structure container was set up. Prior to setting up the structure container, the relaxed structures were mapped back onto the ideal lattice using the mapping functionality of ICET. If a structure could not be mapped correctly, it was left out. This can be seen as a crude structure selection. First, an empty structure container was set up. The mapped reference structures and their potential energies were then used to fill the structure container, making it a collection of all the reference structures together with their cluster vectors.
3. In the next step, the optimizer used for the cluster expansion was determined. ICET supports a variety of fit methods for training the cluster expansion. In order to find the most suitable fitting method, three optimizers were evaluated. The methods used were Automatic Relevance Determination Regression (ARDR), Recursive Feature Elimination (RFE) and Least Absolute Shrinkage and Selection Operator (LASSO). When using the optimizer, the number of reference structures to be used in the training process has to be specified, as well as the number of hyperparameters for the employed fitting method. Suitable values for these parameters were found by minimizing the CV-RMSE.
4. The cluster expansions were now ready to be constructed. Using the reference data in the structure container the effective cluster interactions (ECIs) were trained on this set of data. In the first step, the structures in the structure container were split into two subsets: the training data and the validation data. The training data was used for training the ECIs of the clusters in the cluster space. The second data set was used for validating the predictive power of the cluster expansion. This means that the ECIs acquired from the training set were used in order to predict the eneregis for the structures in the validation set.

The acquired cluster expansions were sampled via MC calculations, in the canonical ensemble and by simulated canonical annealing.

3.4 Sampling the CE in Monte Carlo simulations

For sampling the configuration space of SSZ-13, two different approaches based on the canonical ensemble were used. In both of these cases, the simulations were carried out using the MCHAMMER module in the ICET package. In addition to the regular canonical ensemble, the canonical ensemble supported simulated annealing procedure was used. In all of these simulations, a $2 \times 2 \times 2$ supercell was used. Just as in Metropolis based MC routine, a trial step is taken as in the same manner as in Eq. (2.11), with the density being for a microstate of the canonical ensemble. Due

to the associative nature between Al and the charge compensating proton, the trial step functions had to be rewritten for protonated SSZ-13 (see below). Canonical annealing simulations were performed in order to find the ground state energies for the structures. The annealing simulations, unlike ordinary canonical ensemble simulations, run over a temperature interval. With a cooling function working on the system during the simulation the ground state is more easily obtained than in regular canonical ensemble computations.

3.4.1 Trial swap function for hydrogen

When sampling the configuration space using the canonical ensemble, the trial step function for annealing is identical to the ordinary ensemble. Ordinarily, this functions tries to swap one element in the system with another element on a different site. An example of how this works is that the function randomly picks out a Al site, as well as a random Si site and check whether the swap is energetically favourable. In MCHAMMER, this is implemented for swapping one element at a time, which leads to very low acceptance ratios in the case of the zeolites due to the associative nature of the Al and H.
In order to take this into account, the trial function was rewritten for this purpose. In the case of the chabasite, if an Al atom was to be swapped with a Si atom, the associated OH group which represented the proton had to be swapped as well. In order to this, a list of all 4 oxygen sites related to the T-sites of the structure was created. For every step where a Al would be swapped with a Si, or vice versa, the list was checked to see if there was any OH sites neighbouring the Al site and the same for the O atoms neighboring the Si site. If both of these criteria were fulfilled, a random OH site was picked (if there were more than one) and likewise for the O sites associated with the Si site, and swapped these two as well. Thus, the physicality of the charge compensation was maintained throughout the simulation. It should be noted that not all of the aluminium atoms had neighboring OH. At such an occurance the T-site atoms were allowed to swap sites alone.

3.4.2 Trial swap for divalent counter ions

When Monte Carlo simulations were involving divalent counter ion species the regular swapping method was used. This means that the counter ions were allowed to swap sites, independent of the Al swaps.

4

Binding sites and cluster expansion of proton compensated SSZ-13

In this chapter the results from the Al distribution in SSZ-13 with protons as the counter ion are presented. The chapter will cover the full extent of the procedure used in this thesis, from structure relaxation to construction of the cluster expansions to MC simulations. It also describes finding concerning the binding sites of the protons, which proved to have a significant impact on the energy landscape. To emphasize how the thesis work was carried out, this chapter has been written in chronological order, from finding the proper relaxation method, to looking at the hydrogenic energy contributions depending on the binding sites as well as the energetics stemming from nearest neighbour Al atoms. All of these results were important in the process of being able to obtain an accurate and predictive cluster expansion.

4.1 ReaxFF and DFT

Early on in the project, the method best suited for relaxation of structures were evaluated. To this end, the same set of structures was relaxed using the two different methods presented in the Methodoly chapter. The structures used were from an early version of the project, with structures generated by enumeration over the T-sites only. The database of the structures contained 26 inequivalent structures with an aluminium content which varied from 0 to 4 per primitive unit cell. The structures were relaxed using VASP and LAMMPS. The resulting structures were then compared to each other. In Figure 4.1 the results from these comparisons can be seen. These results suggests that the ReaxFF potential is not suitable for this purpose, since there is a systematic error in the energies for the structures. The energies for the ReaxFF data increases linearly depending on the amount of Al in the cell in comparison to the DFT data. In addition, the energies for each group of structures with the same amount of aluminium in the cell had quite a big spread. The deviations in the groups with the same Al content in the primitive unit cell has a much larger spread for the empirical potential than the ab-initio calculations. In the case of four aluminum in the structure, the energies in the ReaxFF data varied with 5 eV between the lowest and highest energy configurations. Meanwhile, the spread was about 2 eV for the same structures using DFT as the relaxation method. This

further proves the invalidity of the empirical potential. The spread was, however, still large for the structure relaxed by DFT. This big spread could either depend on the protonic binding sites, the aluminum distribution in the structure, had to be sorted out in order to perform a cluster expansion.

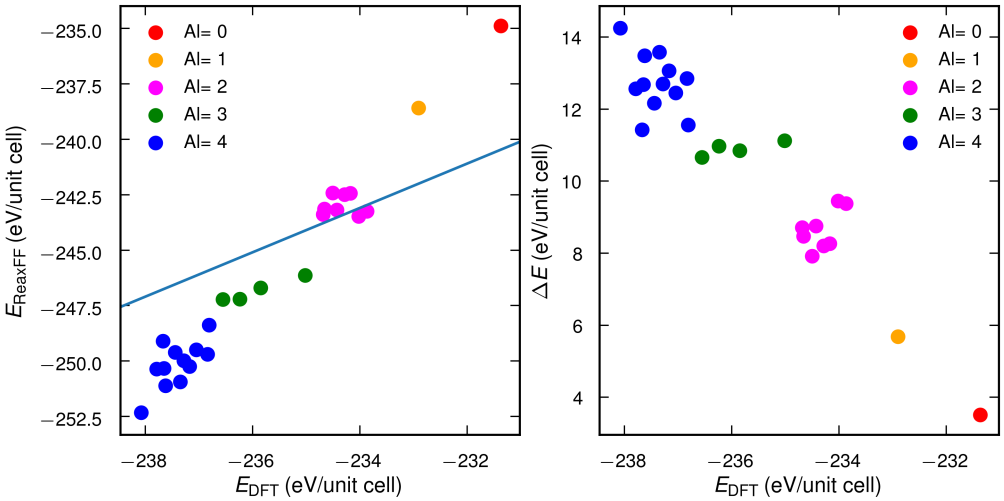

Figure 4.1: The first figure shows the correlation between energies for the same structures relaxed in two different ways: through ReaxFF and DFT. The blue line shows a perfect linear dependence, which is not shown for these structures, suggesting that the ReaxFF potential is not suited for our application. The left figure shows the difference in energy for each structure against the DFT energy. This shows how the energetic difference between the methods increases with the number of aluminium in the structure.

Löwenstein's rule suggest that the energies for structures with Al-Al neighbours should be higher than energies for structures where the Al atoms are separated. In order to sort this out, the same structures from the previous results were used to look at how the energy differs between sets of structures with the same aluminium count in the cell and how many aluminium were neighbouring each other. This was done by looking at the energy of structures as a function of the number of Al nearest neighbours. This can be observed in Figure 4.2. For the structures with 3 and 4 Al in the structure, the lowest energy configurations correspond to structures where Al atoms neighbour each other. These results suggests that Löwenstein's rule actually does not apply, since the nearest neighbour configurations have the lowest energy in the data set. To validate these results, more DFT calculations were needed, with a larger set of structures.

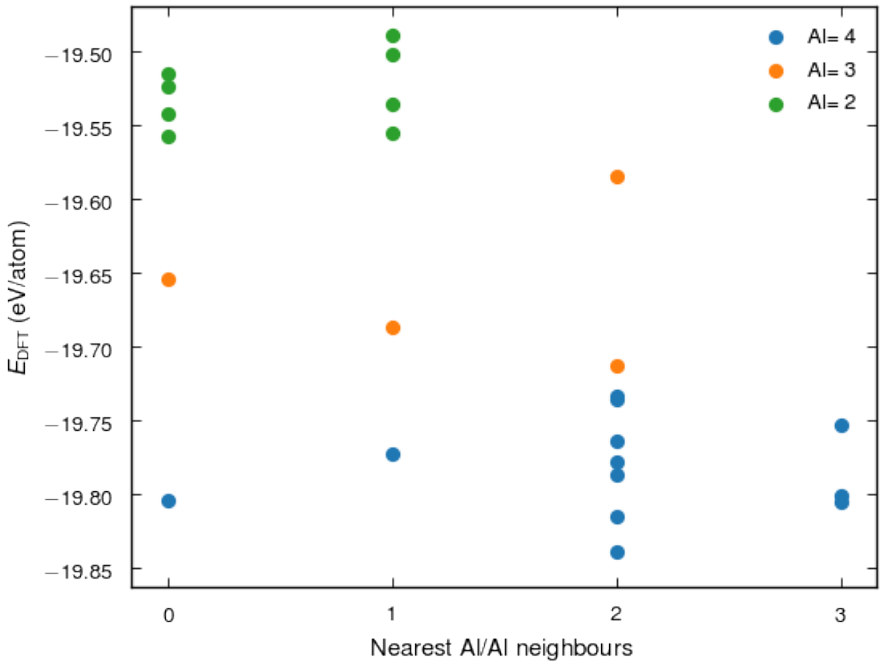

Figure 4.2: This figure shows the energies for different structures as a function of the number of Al-Al nearest neighbours in them. The energies for each structure were obtained using VASP. According to Löwenstein's rule, the structures with Al atoms neighbouring each other should not be the lowest energy lowest energy configuration.

4.2 Energetic contribution of the protonic sites

In order to construct a sensible cluster expansion, the energetic fluctuations in the energy of structures with same chemical compositions had to be sorted out. This was done by looking into the possible binding sites for hydrogen, and scrutinizing how much the energy contribution was from each proton and whether it differed depending on its position in the structure. By using the same aluminium distribution, but varying the hydrogen positions, this could be analyzed. This was done by enumerating the unit cell up to two Al and then distributing the hydrogen to different oxygen sites in the vicinity of Al. In case of structures with 2 Al atoms in the cell, the highest and lowest energies corresponded to the configurations where the aluminium was distributed on the same sites, but with different sites for the protons. These two configurations can be observed in Figure 4.3.

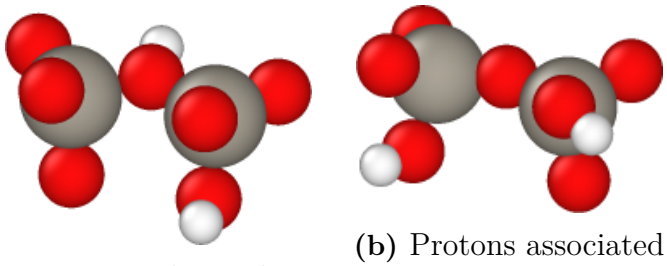

(a) Proton located at bridging oxygen site.

(b) Protons associated with independent oxygen sites.

Figure 4.3: Two different types of protonic binding sites for a unit cell with one pair of Al-Al neighbours. (a)is the lowest energy configuration, while (b) corresponds to the highest energy configuration. The energy difference is about $30.8eV$.

The energy difference for these two sites is about 0.8 eV, which is rather large considering the only difference is the bonding site of the proton. Because of these large energetic contributions, the binding sites had to be taken into account in order to be able to perform an accurate cluster expansion.

To take the protonic site contribution into account, a new enumeration scheme was employed for both T-sites and protonic bonding sites. To this end, the OH was treated as a single species. This enumeration led to many more configurations. By enumerating all possible structures with 1 Al in the primitive unit cell 24 inequivalent structures were acquired. To validate the results from these relaxations, two other functionals were used: namely PBE and PBEsol. The results from these relaxations can be seen in Figure 4.4. These results emphazise the importance of the protonic binding site, showing that it is energetically favourable for the proton to bind in the vicinity relative to the Al atom. The difference is about 1 eV if it binds to a neighbouring O site. Both shear strain and lattice constant of these calculations serve as measure for the degree of structural relaxation. This had been a problem for some of the structures in the earlier DFT calulcations, but for this set of structures this did not occur with any of the functionals.

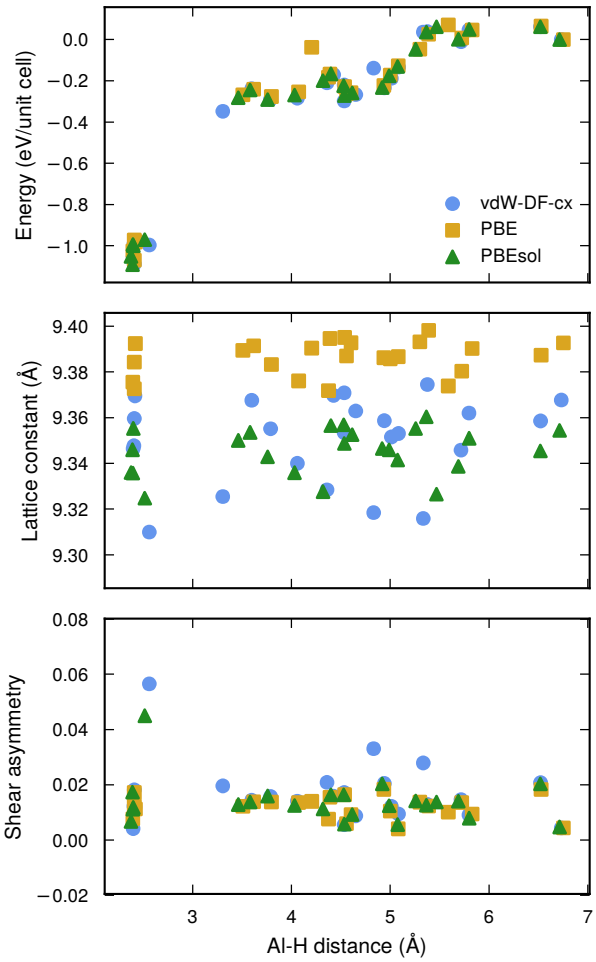

Figure 4.4: Comparison between different XC-functionals for the Al-H distance in the structures generated for the double enumeration scheme. The upper graph shows the energy for each structure relative to the energy of the structure where the protons is the farthest away from the Al. The energies of the structures are similar for all the functionals, while the lattice constant is conserved for the PBE calculations. The shear asymmetry indicates the degree of relaxation. Here, all structures are still relatively close to the ideal structure.

To draw any conclusions whether Löwenstein's rule is applicable, more structures were generated with 2 Al atoms in the primitive unit cell and the same amount of charge compensating H. This generated a total amount of 1572 different configurations. From the previous step, relaxing single Al structures, PBE and PBEsol functionals proved to be much less time consuming, making it much easier to get a high throughput. These functionals were used instead of the vdF-DF-cx method. The PBE based calculations managed to relax a total of 683 structures, while the PBEsol provided 528 configurations. For these two sets of reference structures energy, lattice constant and shear asymmetry were analyzed. In Figure 4.5 these results can be studied. The upper graph clarifies what the results from the first study of Al suggested: Löwenstein's rule is not applicable since many of the low energy configurations corresponds to nearest-neighbour Al atoms.

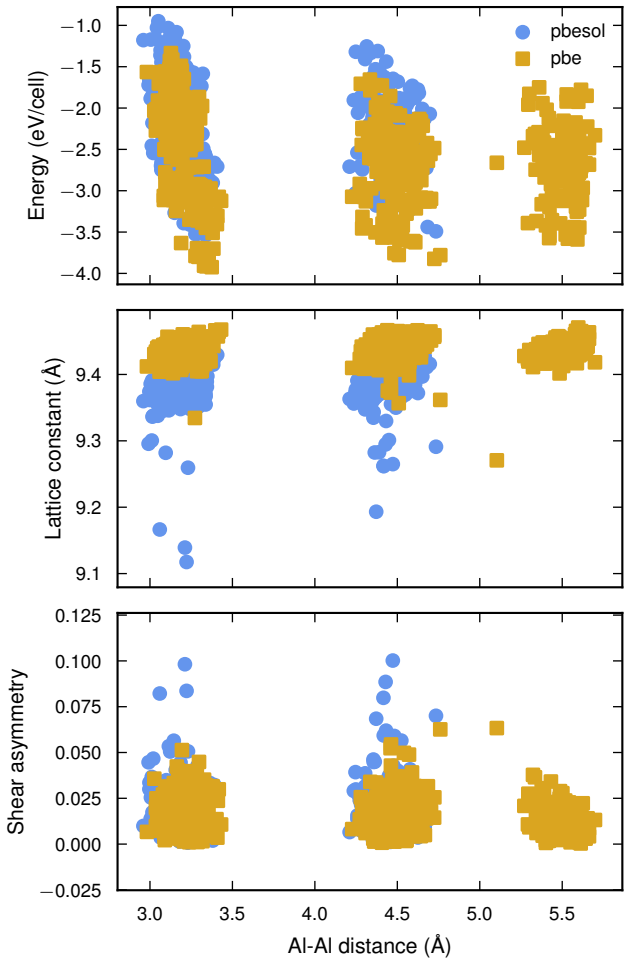

Figure 4.5: Energy, lattice constant and shear asymmetry of the cell with respect to the Al-Al distance for a primitive unit cell with 2 aluminium atoms. The first, second, and third neighbour shell are apparent from the clustering of data points.

4.3 Constructing the cluster expansion

With the hydrogenic contribution to the energy sorted out, a cluster expansion was ready to be constructed. When constructing the cluster expansion, a series of parameters had to be determined in order to get the CV-RMSE value as low as possible. To achieve this, the cutoff radii for each order had to be found, as well as the most suitable fitting method. The latter were examined with respect to the size of the training data set and the parameters present when altering the train size. The dataset used was a combination of the PBE sets described above. This resulted in a total of 708 reference structures.

4.3.1 Learning curves and cutoffs

To begin with, the most effective fitting method had to be found. This was done by comparing the training set size for the different methods used as well as the

convergence with hyper parameters. The latter affect the number of non-zero ECIs in the cluster expansion. Firstly, the effect of training set size was examined. This was done by varying the size of the training size for three different fit methods: ARDR, RFE and LASSO. The results can be seen in Figure 4.6.

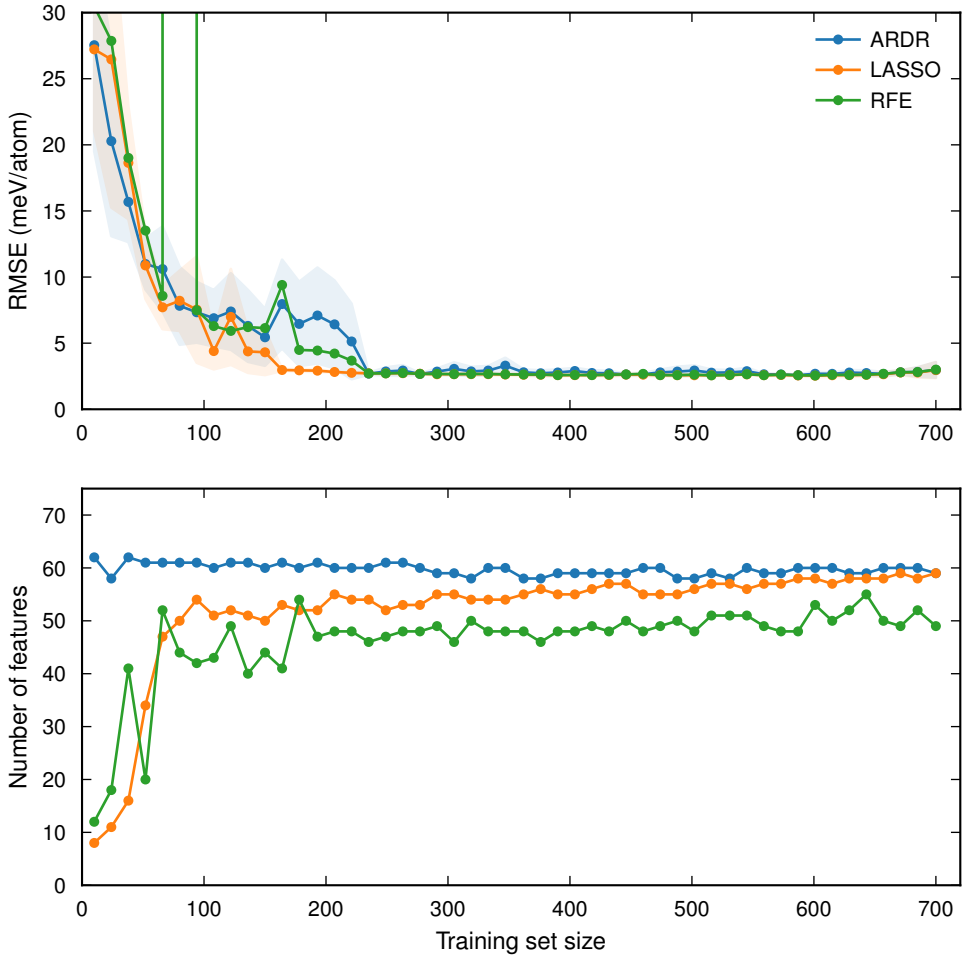

Figure 4.6: Learning curves for the training set size and the number of features in the cluster expansion. The RMSE converges at approximately 250 reference structures. The performance of the different fit methods is almost identical with regard to the training set size.

Next, suitable cutoffs for the cluster expansion had to be found. This was done by first varying the radius for pairs in an interval between 3.7 and 9 Å. and then looking at triplets with cutoff radii of 3.7 and 5 Å. The cluster space achieved the lowest RMSE with cutoffs radii of 5 and 3.7 Åfor pairs and triplets, respectively. Even though it showed a better RMSE for higher cutoffs it showed a volatile behavior and thus discarded. The final RMSE of 2.9 meV/atom is very low when compared

to the range of input energies.

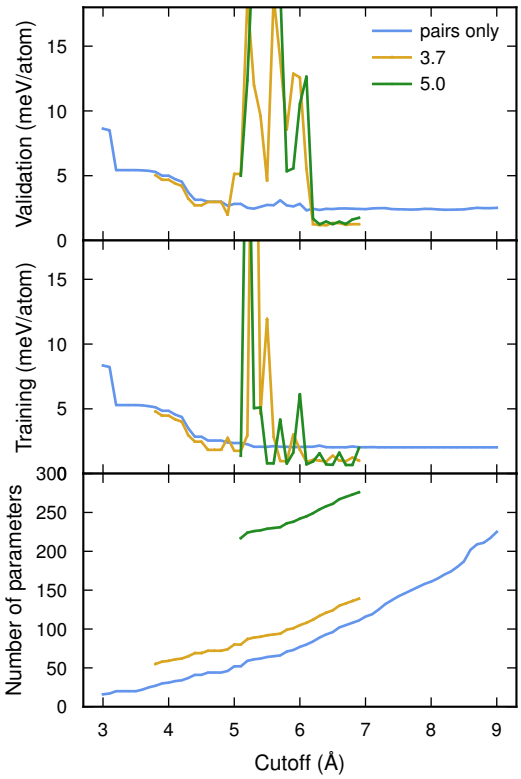

Figure 4.7: Cluster space convergence with respect to cutoff radii for pairs and triplets. The upper panel shows the validation RMSE, the middle panel shows the training RMSE, and the bottom panel exhibits the number of non-zero parameters.

4.4 Cluster expansion and ECIs

The ARDR method was used for fitting the final cluster expansion. The ECIs acquired can be seen observed in Figure 4.8. This shows the interaction between the pair in the cluster space. The ECIs are not based on the mixing energy for the structures, but rather a shifted total energy. This shifted total energy was calculated as

$$E_{\mathrm{CE}} = \frac{E_s}{n_s} - \frac{E_r}{n_r}, \tag{4.1}$$

where s is the current structure, r the reference structure (pure silicalite) and n is the number of atoms in each of these structures.

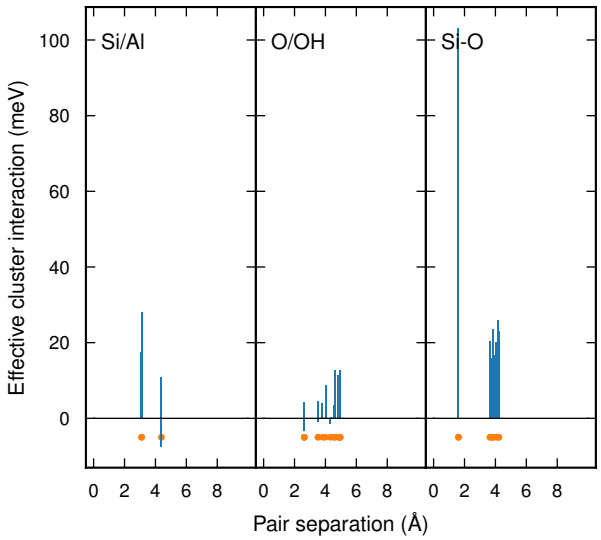

Figure 4.8: ECIs for the pairs in the system.

To visualize the performance of the CE its predictions were compared with the reference data. This done by looking at the correlation between the predicted energies of the structures as well as the reference energies. This comparison can be seen in figure 4.9.

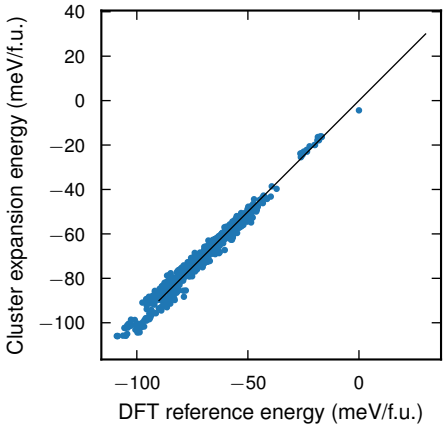

Figure 4.9: The correlation between the reference structures and the cluster expansion.

4.5 Monte Carlo simulations

The sampling of the resulting cluster expansion is presented in this section. In these simulations a supercell of $2 \times 2 \times 2$ the size of the primitive unit cell was used, containing a total amount of 96 T-sites and 288 atoms in the structure. These simulations were carried out using the canonical ensemble, and the properties of interest were the average energies as well as the aluminium distribution. In addition, the associative behaviour between the Al atoms and the protons were examined.

4.5.1 Convergence and energies

For the MC runs 10000 trial steps were taken for each atomic site in the structure, resulting in a total of 288000 steps. This was done for 8 different concentrations of Al and at 4 different temperatures. The concentrations ranged from 2 up to 16 Al atoms in the supercell, including only even numbers of aluminium atoms. The temperatures used were 300, 600, and 900 K. Canonical annealing simulations were also performed for the same Al concentrations using a cooling function where the temperature decreased from 1800 to 300 K. A comparison between the canonical annealing and ensemble simulations were done for structures containing 2 and 14 Al. The comparison can be observed in Figure4.10. As the figure suggests the usage of the canonical ensemble is better suited for the MC calculations, due to the fact that the canonical ensemble reaches the ground state earlier on and they also have a lower energy.

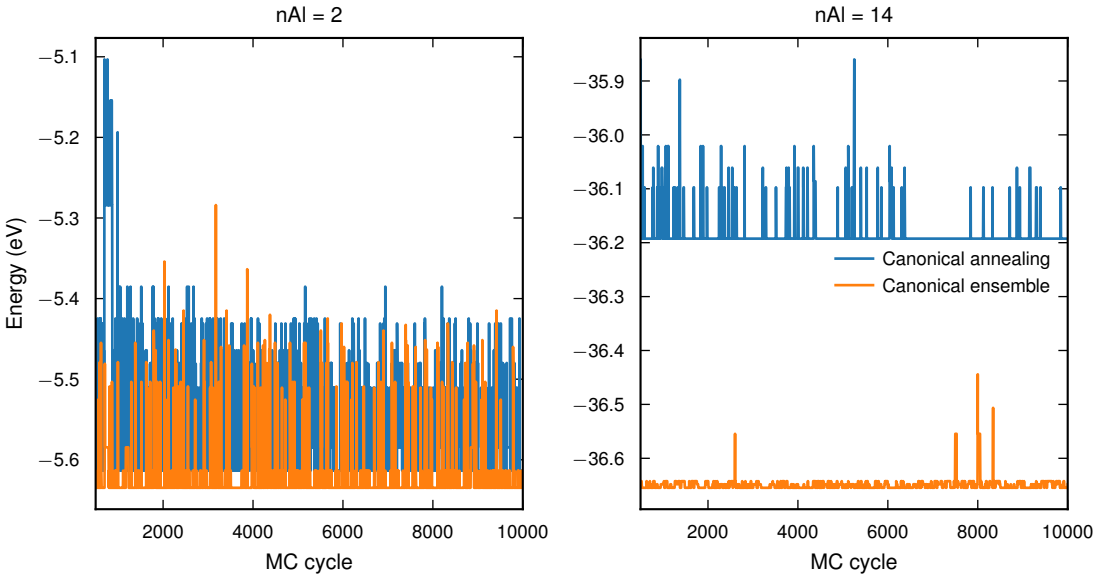

Figure 4.10: Comparison between simulations using canonical annealing and canonical ensemble for two different Al concentrations. The canonical ensemble data is taken from the simulations set at $T = 300$ K.

The energies from the canonical ensemble simulations were then averaged over the length of the simulations. By comparing the averaged energies with the concentration of Al for different temperatures, a linear dependence of the energies was found. This was the expected result of the concentration dependence of the energy, due to how the energies of the structures were normalized in the cluster expansion. This can be observed in Figure 4.11

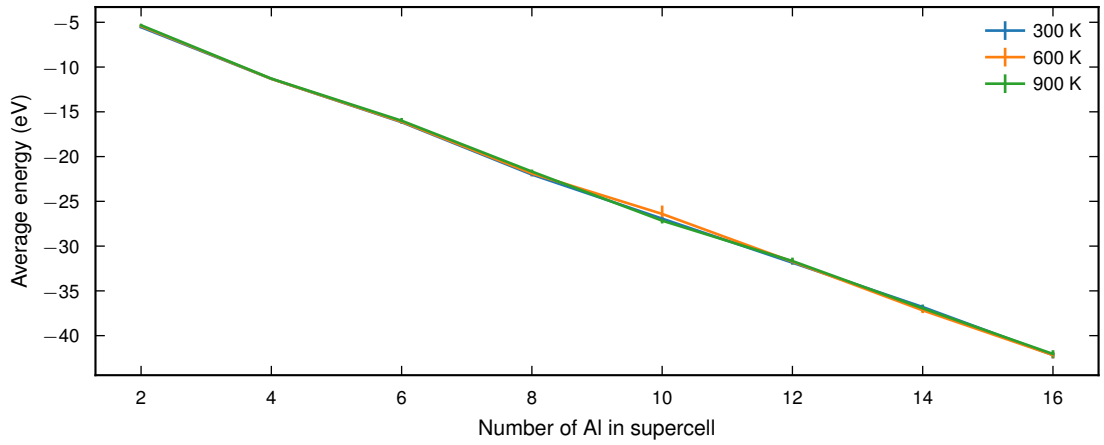

Figure 4.11: Average energy as a function of the Al-Al concentration of the simulations in the canonical ensemble.

The energy relative to the Al-Al distance and the probability distribution for the MC simulations containing two aluminium were investigated. This can be observed in figure 4.12. This shows that is highly favourable for H-SSZ13 to disobey Lẅoenstein's rule, and thus letting the Al atoms to neighbour eachother. The aluminium also swaps sites constantly during the simulation, even though it has been equilibrated.

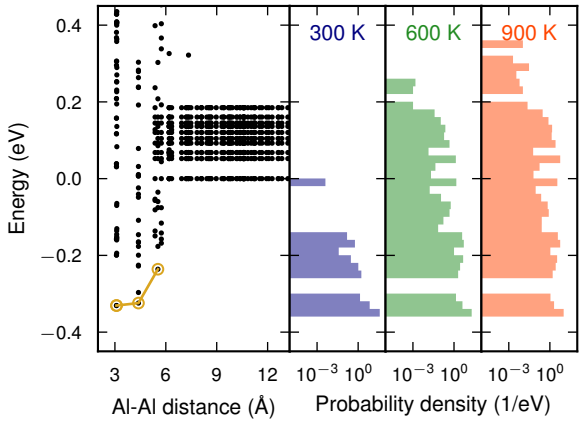

Figure 4.12: The energy in relation to the Al-Al distance and the probabilites of the different states at temperatures of 300 K, 600 K and 900 K.

4.5.2 Clustering of aluminium

Given that the canonical ensemble simulations are sufficient for finding the ground state they were used further. To this end, pairs were assigned to neighbour shells as shown in Figure 4.13. The cutoffs used for observing the pairs of each order can be seen in table 4.1.

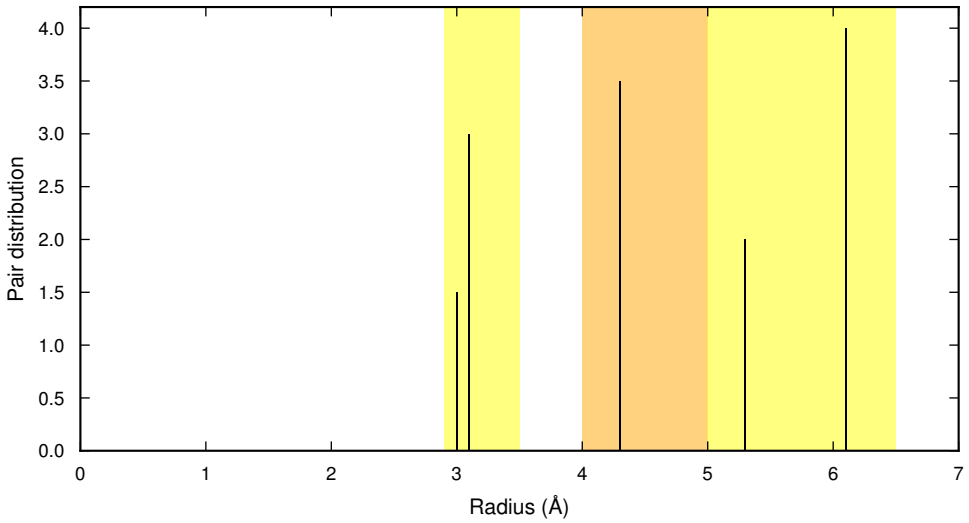

Figure 4.13: Si-Si pair distribution of the pure silicalite. The yellow field indicates the cutoffs used when counting the pairs.

Table 4.1: The different cutoffs used to observe Al-Al pairs of certain orders.

Order	$r_{\min}$ (Å)	$r_{\max}$ (Å)
First	2.9	3.5
Second	4.0	5.0
Third	5.0	6.5

The clustering of Al-Al nearest neighbours in the MC simulations were examined, which means that the clustering effect for different temperatures were accounted for. The clustering was averaged only for the nearest-neigbour Al-Al pair. This can be observed in figure placeholder. This suggests that clustering is beneficial for the protonated SSZ-13 is beneficial at almost all temperatures. This was done with a counting function which utilize did not utilize self-interaction of the species. This shows that Al-Al neighbors forms at all temperatures in protonated SSZ-13.

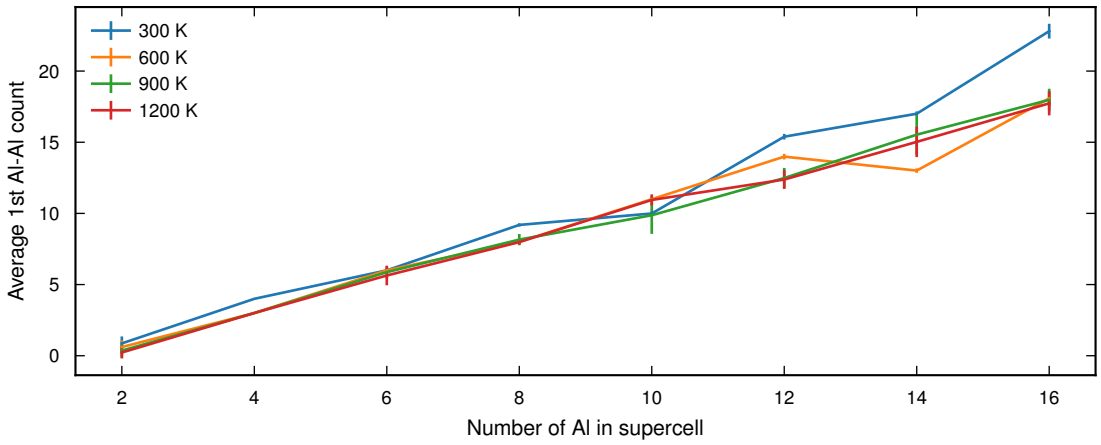

Figure 4.14: Average count of Al-Al first nearest neighbours in regard of the amount of Al in the supercell. This shows that clustering is favourable for the aluminium.

5

Divalent counter ions

To see whether Löwenstein's rule was violated for other type of counter ions, charge compensating divalent species were examined. In this chapter the results from the structures charge compensated with divalent cations are presented. The construction of the cluster expansions followed a similar procedure as for H-SSZ-13 and as is not described further. The different counterion species are presented in the order of groups in the periodic table. First off are the alkaline earth metals in descending order and then copper and zinc. In all of these cases, ARDR was found to be the optimal fit method. Due to almost identical geometries for the cases for the divalent cations, the cluster radius was found to achieve the lowest RMSE at 6 Åfor pairs only. This will be shown in the magnesium case, but for the other individual cases the same procedure was used and the same optimal cutoff was acquired.

5.1 Magnesium compensated structures

When relaxing the structures compensated with Mg^{2+}, 405 structures managed to converge. Out of these, 375 were succesfully mapped on their original configurations. The DFT energies were compared with the Al-Al distance for the structures containing two aluminum atoms. This can be observed in Figure 4.2. This suggests that non-Löwensteinian configurations have lower energies.

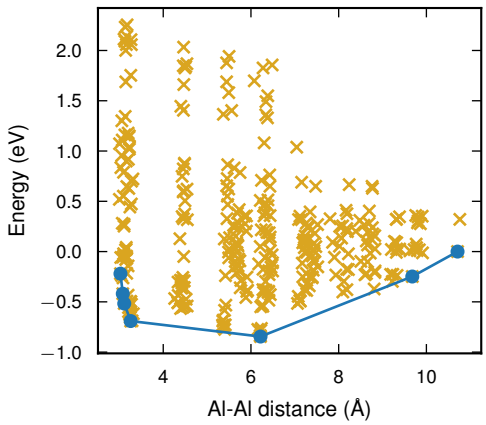

Figure 5.1: The reference energies relative to the Al-Al pair distances for Mg^{2+}

The mapped structures were then used in order to find the optimal cutoffs for the divalently compensated systems. The cluster space convregence for different cutoffs

can be observed in Figure 5.2. The minimal RMSE was found for pairs only at 6 Å. Thereafter, the cluster expansion was performed using the ARDR fit method. The resulting ECIs can be seen in 5.3.

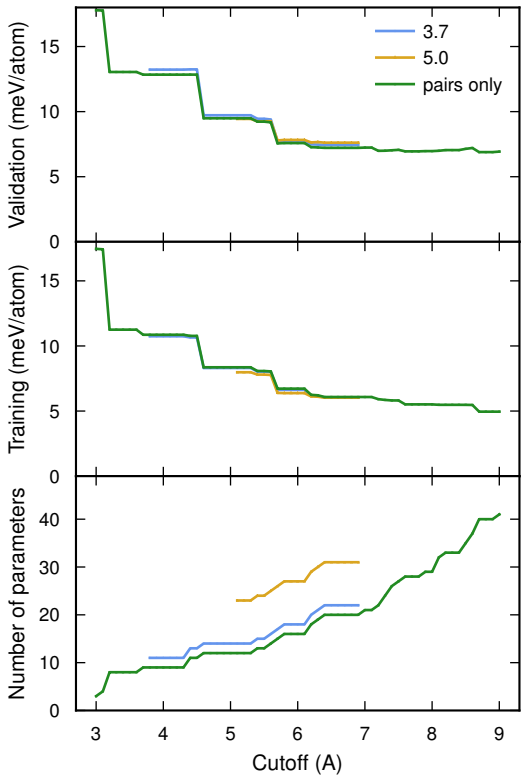

Figure 5.2: The cluster space convergence for Mg^{2+} as the counter ion.

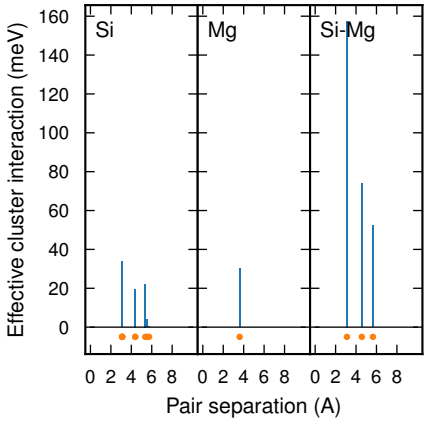

Figure 5.3: The ECIs for the magnesium compensated structures.

The ECIs were sampled using the canonical ensemble for three different temperatures: 600, 900 and 1200 K. All of these simulations were done in supercell of the same dimensions as in the proton case and for a total of 20000 trial steps. The simulations were considered to be equilibrated at 2000 steps, leaving the steps prior out

from the averaging. The energetic contribution in regard of the Al-Al distance can be seen in Figure 5.4. These results suggests that structures abiding Löwenstein's rule are thermodynamically more favourable. Violations of the rule does however occur at all temperatures used in these computations.

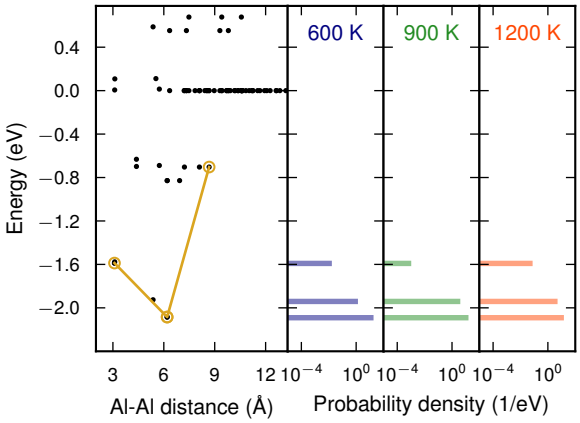

Figure 5.4: The energetic contribution in regard of the Al-Al distance of the simulation. The probability density for different temperatures can be seen in the right part of the figure.

5.2 Calcium counter ions

The same procedure was done for Ca^{2+} as the counter ion. Out of 324 relaxed reference structures, 319 could be mapped onto their original configurations. The energies of the structures were plotted as a function of the aluminum pair distance for the structures containing 2 Al. This is shown in Figure 5.5a. The cluster expansion was carried out in the same manner as for Mg^{2+}. The energy in regard of the Al-Al distance can be seen in Figure 5.5b, together with the probability density for three different temperatures. In this case, the non-Löwensteinian configuration is not visited for any of the temperatures.

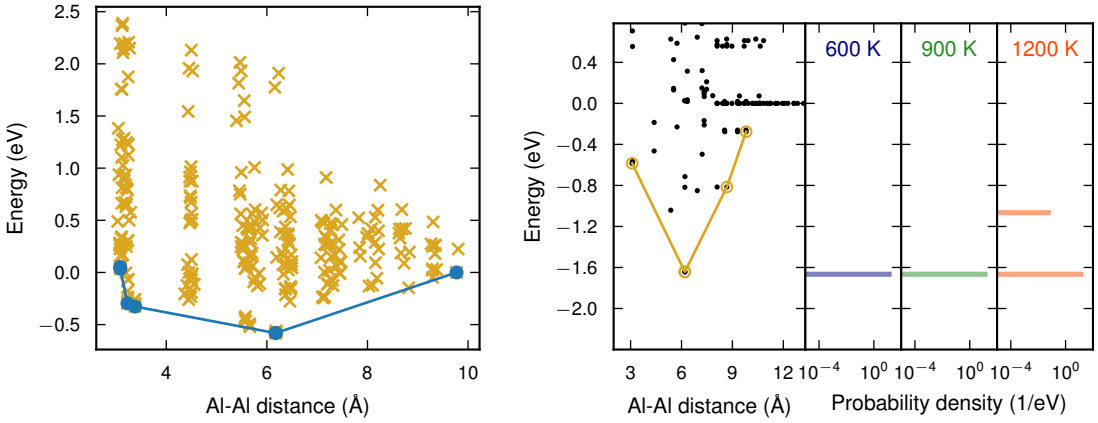

(a) DFT energies. **(b)** MC energies and densitites.

Figure 5.5: The energetic contribution in regard of the Al-Al distance for the DFT and MC data. Probability densities for the different energies and different temperatures can be observed for the MC simulations.

5.3 Strontium as counter ion

The next counter ion species to be examined was Sr^{2+}. 405 structures converged in the relaxation, and out of these 400 managed to be mapped onto their original configurations. The relaxed energies were plotted as a function of the aluminum distance. This can be observed in Figure 5.6a. The MC simulation took place suing the same arrangement as for the other divalently compensated structures. The resulting energies relative to the Al-Al distance can be observed in Figure 5.6b. Löwenstein's rule is not violated in any of these simulations, just as for Ca^{2+} compensated SSZ-13.

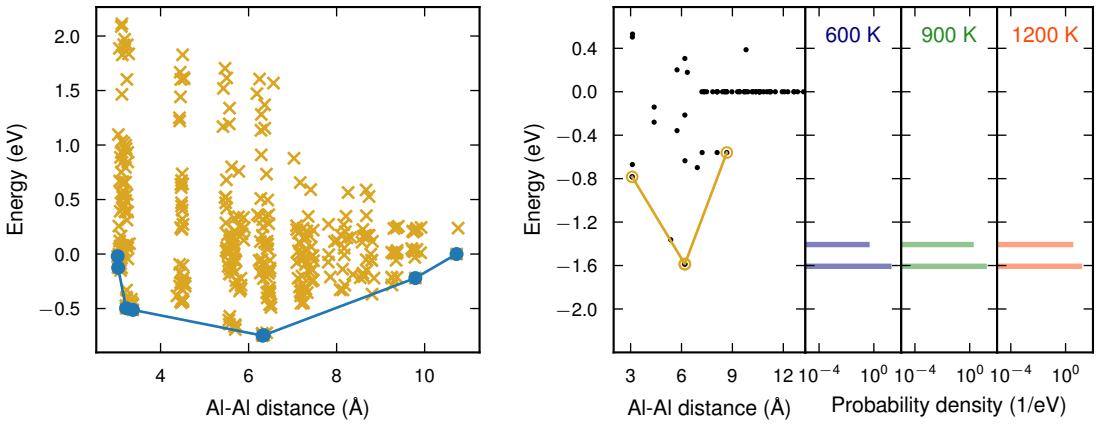

(a) DFT energies. **(b)** MC energies and densitites.

Figure 5.6: The energetic contribution in regard of the Al-Al distance for the DFT and MC data for Sr^{2+} compensated structures containing two Al. Probability densities for the different energies and different temperatures can be observed for the MC sumilations.

5.4 Barium compensated structures

For Ba^{2+} compensated zeolites 404 structures was succesfully relaxed. Out of these 357 structures was able to be mapped onto their origin configurations. The DFT energies relative to the aluminium distances can be seen in figure 5.7a. Figure 5.7b suggests that nearest neighbour Al-Al do occur at higher temperatures for Ba^{2+} compensated structures.

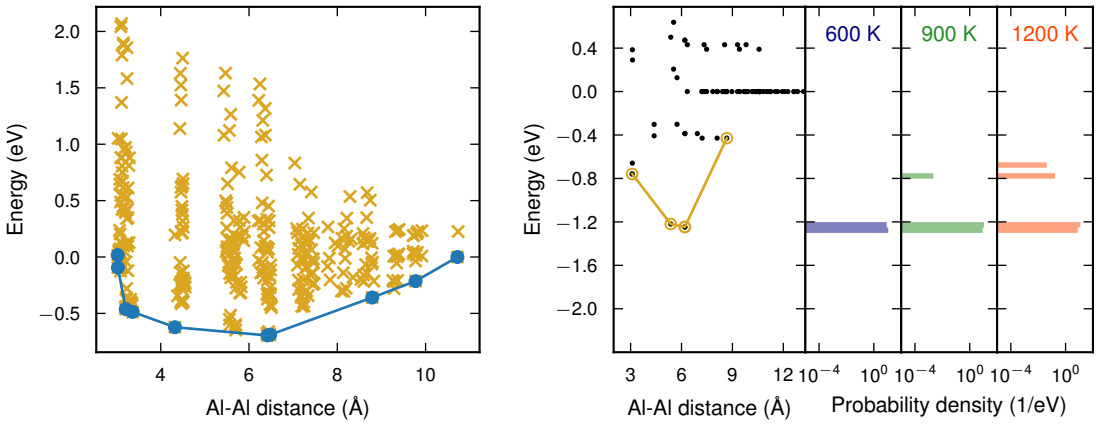

(a) DFT energies. **(b)** MC energies and densities.

Figure 5.7: The energies for the DFT and MC simulations. The MC data depicts the energy states visited throughout the simulation a tthe different temperatures.

5.5 Copper counter ions

With Cu^{2+} as the charge compensating counter ion, all of the 517 relaxed structures managed to be mapped onto their unrelaxed forms. The reference energies as a function to the Al-Al distance for each structure can be observed in Figure 5.8a. The resulting MC energies and probability densites can be seen in Figure 5.8b. Just as the DFT energies shows, Al-Al nearest neighbours occurs at high frequency.

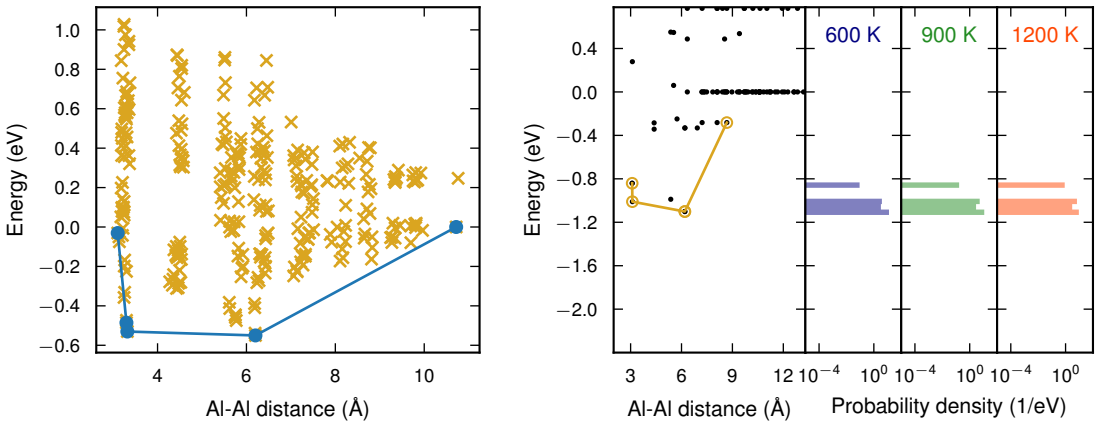

(a) DFT energies. **(b)** MC energies and densities.

Figure 5.8: The energies in relation to the distance between aluminum pairs for both the converged reference structures and the MC simulations. The occupied energy states can be seen in the right of 5.8b.

5.6 Zinc compensated structures

405 Zn^{2+} compensated structures managed to converge during the relaxation. The energies for these in regard of the Al-Al distance can be observed in Figure 5.9a. These results show that breaking Löwenstein's rule does not correspond to the lowest energy. 394 of the relaxed structures were successfully mapped and used in the CE. From the MC simulations, this configuration is however visited at temperatures of 900 K and higher. This can be observed in Figure 5.9b.

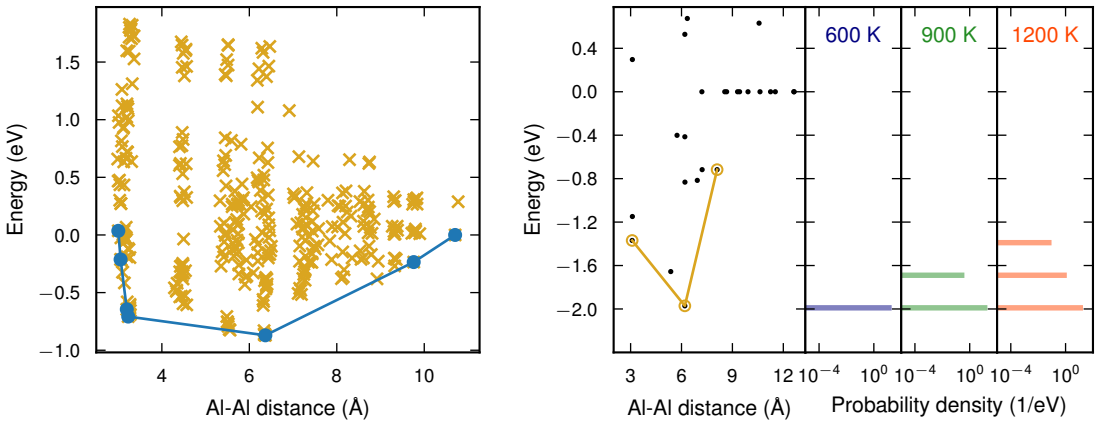

(a) DFT energies. **(b)** MC energies and densites.

Figure 5.9: The DFT and MC simulation energies for zinc compensated structures. The latter simulations show the probability density for the different temperatures.

5.7 Compilation and comparisons between divalently compensated SSZ-13

The lowest energy configurations in regard of the Al-Al distance for the divalent counter ion species were compiled together. In Table 5.1 the different counter ion species and whether they violate Löwenstein's rule for certain temperatures have been compiled together.

Table 5.1: Violations of Löwenstein's rule in regard of counter ion species and temperature.

Counter ion	600 K	900 K	1200 K
Mg^{2+}	Yes	Yes	Yes
Ca^{2+}	No	No	Yes
Sr^{2+}	No	No	No
Ba^{2+}	No	Yes	Yes
Cu^{2+}	Yes	Yes	Yes
Zn^{2+}	No	No	Yes

In Figure 5.10 an overview of the energetics in respect of the Al-Al distance for the different counter ions can be observed. No real conclusions can be drawn from these compilations. The energy difference between first and higher order neighbours does not indicate whether the rule is prone to be violated for the divalently compensated structures.

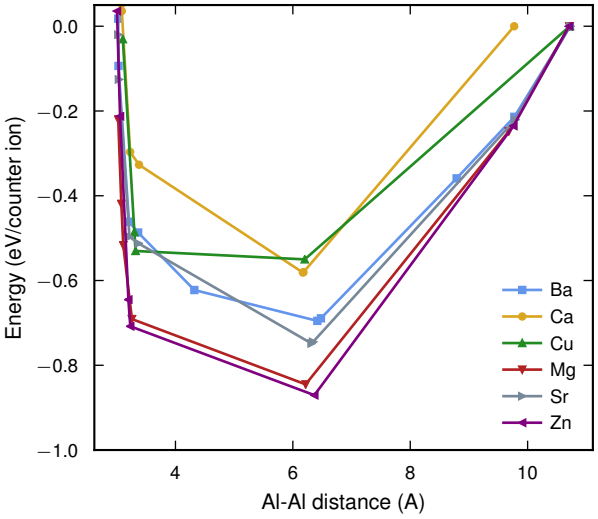

Figure 5.10: Energy as a function the Al-Al distance for the divalently compensated structures.

Lastly, the interaction strength between the Al-Al neighbours was calculated. These calculations were based upon the results from the MC simulations. This is shown in Figure 5.11.

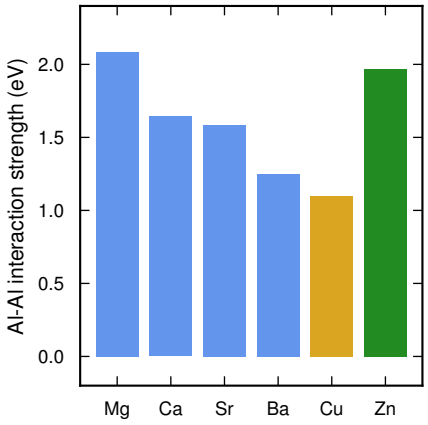

Figure 5.11: Interaction strengths between Al-Al atoms in regard of the divalent counter ions compensating the system.

6
Discussion

In this chapter the results of the thesis are discussed, together with useful insights that have been gathered throughout this thesis work. Furthermore, it will also discuss the motivation of tools used in the project and what future endeavours within the field of zeolites can benefit from this thesis as well as how a natural continuation of this thesis could be pursued.

6.1 Relaxation process

During the first months of the thesis the ReaxFF potential created by Bai et al. [24] was used in a large extent. This was due to the fact that the initial DFT calculations of the SSZ-13 systems probed tedious to relax with large problems with getting the energies and forces of the structure to converge. When the legitimacy of the reaction force field potential was refuted, the only resort was to use DFT in order to collect the needed reference data. Comparing the different functionals in order to check for the validity of the vdF-DF-cx functional proved to be very fruitful in this, since it provided a much faster way of relaxing the structures using PBE as the exchange-correlation functional. This also shows that high throughput DFT simulations are possible for rather complex molecular systems as SSZ-13.

6.2 Cluster expansions

Initially, the main purpose of this thesis was to look whether cluster expansions could be an option for studying rather complex molecular structures. This has already been proven for the case of clathrates, but the succesful employment of cluster expansions in this thesis further reinforces how powerful a tool cluster expansions can be when used correctly. Due to the efficiency of cluster expansions in combination with sampling them in Monte Carlo simulations Löwenstein's rule could be dismissed as a universal rule for charge compensated zeolites.

6.3 Löwenstein's rule

Although violations of Löenstein's rule has been observed before [10], the extent of how and to what degree this happens has not before been proved. Although non-Löwensteinian configurations have the lowest energy for SSZ-13 compensated with the divalent counter ions examined in this thesis, many of them still proved to exhibit

Al-Al nearest neighbours throughout the MC simulations. The most interesting case is probably for Cu^{2+}, since structures compensated with it violated the rule at all of the temperatures. The case of protonated SSZ-13 is also interesting, since the lowest energy configuration does not obey Löwenstein's rule.
The main difference between protonated and divalently compensated SSZ-13 is the locality of the counter charge. In the case of H^+ as the counter ion, the charge compensation occurs in the close vicinity of the Al, making the pair act as a dipole. In the case of the divalent atoms, the interstitial binding site makes the charge compensation not as local as for the protonated case. This is probably the cause to the fact that non-Löwensteinan structures aren't that probable for divalently compensated structures. This can clearly be seen in the relaxed data for all of the divalent species, since none of them shows that the most favourable structure violates Löwenstein's rule.

6.4 Future research

Both Cu^{2+} and H^+ compensated zeolites are widely used as zeolitic catalysts [2] [32]. It would be interesting to study catalytic behaviour for zeolitic structures disobeying Löwenstein's rule. Sodium is the most common counter ion species used in zeolite synthesis, so using the same computational methodology as done in this thesis would be very interesting. This was actually pursued, but the binding sites for Na^+ counterions could not be determined to a reasonable extent, disabling the usage of cluster expansions to study the different energetics of sodium compensated configurations.

7
Conclusion

One of the main purposes of the project was to see if cluster expansions could be employed for zeolites, complex systems compared to the binary alloys that are the most common system performing this technique. When it comes to the amount of reference structures needed in order to do the cluster, zeolithic systems seem to need more of these than for simpler systems to get a high enough accuracy of the RMSE. This thesis has managed to give a detailed view of how Löwenstein's rule is not always applicable for charge compensated zeolites. It has also shown that DFT calucations of large amount of zeolitic structures, are possible. The PBE functional proved to be able to handle these complex very efficiently, showing that high throughput calculations can be acquired for these systems. This has been shown for various counter ions. From the MC simulations, it has been shown that the rule is disobeyed for the following charge compensating species: H^+, Mg^{2+}, Ba^{2+}, Cu^{2+} and Zn^{2+}. Using these insights for catalytic computations would be highly interesting. Investigating the affect of Na^+ and other monovalent counterions for charge compensation could bring useful insights on how the Al is distributed throughout the synthesis of zeolites.

Bibliography

[1] G. Diego Gatta and Paolo Lotti. "Chapter 1 - Systematics, crystal structures, and occurrences of zeolites". In: *Modified Clay and Zeolite Nanocomposite Materials*. Ed. by Mariano Mercurio, Binoy Sarkar, and Alessio Langella. Micro and Nano Technologies. Elsevier, 2019, pp. 1–25. ISBN: 978-0-12-814617-0. DOI: https://doi.org/10.1016/B978-0-12-814617-0.00001-3. URL: http://www.sciencedirect.com/science/article/pii/B9780128146170000013.

[2] Yi Li, Lin Li, and Jihong Yu. "Applications of Zeolites in Sustainable Chemistry". In: *Chem* 3.6 (2017), pp. 928–949. ISSN: 2451-9294. DOI: https://doi.org/10.1016/j.chempr.2017.10.009.

[3] J Weitkamp. "Zeolites and Catalysis". en. In: *Solid State Ionics* 131.1-2 (June 2000), pp. 175–188. ISSN: 01672738. DOI: 10.1016/S0167-2738(00)00632-9.

[4] Mark E. Davis. "Zeolites and Molecular Sieves: Not Just Ordinary Catalysts". en. In: *Industrial & Engineering Chemistry Research* 30.8 (Aug. 1991), pp. 1675–1683. ISSN: 0888-5885, 1520-5045. DOI: 10.1021/ie00056a001.

[5] D.E.W. Vaughan. "The Roles of Metal and Organic Cations in Zeolite Synthesis". en. In: *Studies in Surface Science and Catalysis*. Vol. 65. Elsevier, 1991, pp. 275–286. ISBN: 978-0-444-89088-7. DOI: 10.1016/S0167-2991(08)62912-2.

[6] Jiří Čejka. *Introduction to Zeolite Science and Practice*. 3rd rev. ed. Vol. Studies in surface science and catalysis. Amsterdam: Elsevier, 2007. ISBN: 0-444-53063-0.

[7] Marie Jeffroy, Carlos Nieto-Draghi, and Anne Boutin. "New Molecular Simulation Method To Determine Both Aluminum and Cation Location in Cationic Zeolites". en. In: *Chemistry of Materials* 29.2 (Jan. 2017), pp. 513–523. ISSN: 0897-4756, 1520-5002. DOI: 10.1021/acs.chemmater.6b03011.

[8] Brandon C. Knott et al. "Consideration of the Aluminum Distribution in Zeolites in Theoretical and Experimental Catalysis Research". In: *ACS Catalysis* 8.2 (2018), pp. 770–784. DOI: 10.1021/acscatal.7b03676. eprint: https://doi.org/10.1021/acscatal.7b03676. URL: https://doi.org/10.1021/acscatal.7b03676.

[9] Lin Chen et al. "Effect of Al-distribution on oxygen activation over Cu–CHA". In: *Catal. Sci. Technol.* 8 (8 2018), pp. 2131–2136. DOI: 10.1039/C8CY00083B. URL: http://dx.doi.org/10.1039/C8CY00083B.

[10] Rachel E. Fletcher, Sanliang Ling, and Ben Slater. "Violations of Löwenstein's Rule in Zeolites". en. In: *Chem. Sci.* 8.11 (2017), pp. 7483–7491. ISSN: 2041-6520, 2041-6539. DOI: 10.1039/C7SC02531A.

[11] Veronique Van Speybroeck et al. “Advances in theory and their application within the field of zeolite chemistry”. In: *Chem. Soc. Rev.* 44 (20 2015), pp. 7044–7111. DOI: 10.1039/C5CS00029G. URL: http://dx.doi.org/10.1039/C5CS00029G.

[12] A. M. Beale et al. “Recent Advances in Automotive Catalysis for NO_x Emission Control by Small-Pore Microporous Materials”. en. In: *Chemical Society Reviews* 44.20 (2015), pp. 7371–7405. ISSN: 0306-0012, 1460-4744. DOI: 10.1039/C5CS00108K.

[13] Laura Regli et al. “Acidity properties of CHA-zeolites (SAPO-34 and SSZ-13): an FTIR spectroscopic study”. In: *Oxide Based Materials*. Ed. by Aldo Gamba, Carmine Colella, and Salvatore Coluccia. Vol. 155. Studies in Surface Science and Catalysis. Elsevier, 2005, pp. 471–479. DOI: https://doi.org/10.1016/S0167-2991(05)80174-0. URL: http://www.sciencedirect.com/science/article/pii/S0167299105801740.

[14] Dustin W. Fickel and Raul F. Lobo. “Copper Coordination in Cu-SSZ-13 and Cu-SSZ-16 Investigated by Variable-Temperature XRD”. In: *The Journal of Physical Chemistry C* 114.3 (2010), pp. 1633–1640. DOI: 10.1021/jp9105025. eprint: https://doi.org/10.1021/jp9105025. URL: https://doi.org/10.1021/jp9105025.

[15] R.K. Pathria and Paul D. Beale. “The Canonical Ensemble”. en. In: *Statistical Mechanics*. Elsevier, 2011, pp. 39–90. ISBN: 978-0-12-382188-1.

[16] Jos Thijssen. *Computational Physics*. en. 2nd ed. Cambridge: Cambridge University Press, 2007. ISBN: 978-1-139-17139-7.

[17] N. Metropolis et al. “Equation of State Calculations by Fast Computing Machines”. In: 21 (June 1953), pp. 1087–1092. DOI: 10.1063/1.1699114.

[18] Richard M. Martin. *Electronic Structure: Basic Theory and Practical Methods*. Cambridge University Press, 2004. DOI: 10.1017/CBO9780511805769.

[19] J.M. Sanchez, F. Ducastelle, and D. Gratias. “Generalized Cluster Description of Multicomponent Systems”. en. In: *Physica A: Statistical Mechanics and its Applications* 128.1-2 (Nov. 1984), pp. 334–350. ISSN: 03784371. DOI: 10.1016/0378-4371(84)90096-7.

[20] Axel van de Walle. “Multicomponent Multisublattice Alloys, Nonconfigurational Entropy and Other Additions to the Alloy Theoretic Automated Toolkit”. en. In: *Calphad* 33.2 (June 2009), pp. 266–278. ISSN: 03645916. DOI: 10.1016/j.calphad.2008.12.005.

[21] Mattias Ångqvist et al. “ICET – A Python Library for Constructing and Sampling Alloy Cluster Expansion”. In: *Draft* (2019).

[22] Ask Hjorth Larsen et al. “The atomic simulation environment—a Python library for working with atoms”. In: *Journal of Physics: Condensed Matter* 29.27 (June 2017), p. 273002. DOI: 10.1088/1361-648x/aa680e. URL: https://doi.org/10.1088%2F1361-648x%2Faa680e.

[23] Ch. Baerlocher and L.B. McCusker. “Database of Zeolite Structures”. In: (). URL: http://www.iza-structure.org/databases/.

[24] Chen Bai, Lianchi Liu, and Huai Sun. “Molecular Dynamics Simulations of Methanol to Olefin Reactions in HZSM -5 Zeolite Using a ReaxFF Force

Field". In: *The Journal of Physical Chemistry C* 116 (Mar. 2012), pp. 7029–7039. DOI: 10.1021/jp300221j.

[25] Steve Plimpton. "Fast Parallel Algorithms for Short-Range Molecular Dynamics". In: *Journal of Computational Physics* 117.1 (1995), pp. 1–19. ISSN: 0021-9991. DOI: https://doi.org/10.1006/jcph.1995.1039. URL: http://www.sciencedirect.com/science/article/pii/S002199918571039X.

[26] G. Kresse and J. Furthmüller. "Efficient Iterative Schemes for Ab Initio Total-Energy Calculations Using a Plane-Wave Basis Set". In: *Physical Review B* 54.16 (Oct. 15, 1996), pp. 11169–11186. DOI: 10.1103/PhysRevB.54.11169. URL: https://link.aps.org/doi/10.1103/PhysRevB.54.11169 (visited on 05/31/2019).

[27] G. Kresse and J. Furthmüller. "Efficiency of Ab-Initio Total Energy Calculations for Metals and Semiconductors Using a Plane-Wave Basis Set". In: *Computational Materials Science* 6.1 (July 1, 1996), pp. 15–50. ISSN: 0927-0256. DOI: 10.1016/0927-0256(96)00008-0. URL: http://www.sciencedirect.com/science/article/pii/0927025696000080 (visited on 05/31/2019).

[28] R. O. Jones and O. Gunnarsson. "The Density Functional Formalism, Its Applications and Prospects". en. In: *Reviews of Modern Physics* 61.3 (July 1989), pp. 689–746. ISSN: 0034-6861. DOI: 10.1103/RevModPhys.61.689.

[29] Kristian Berland and Per Hyldgaard. "Exchange functional that tests the robustness of the plasmon description of the van der Waals density functional". In: *Phys. Rev. B* 89 (3 Jan. 2014), p. 035412. DOI: 10.1103/PhysRevB.89.035412. URL: https://link.aps.org/doi/10.1103/PhysRevB.89.035412.

[30] John P. Perdew, Matthias Ernzerhof, and Kieron Burke. "Rationale for Mixing Exact Exchange with Density Functional Approximations". en. In: *The Journal of Chemical Physics* 105.22 (Dec. 1996), pp. 9982–9985. ISSN: 0021-9606, 1089-7690. DOI: 10.1063/1.472933.

[31] John P. Perdew et al. "Restoring the Density-Gradient Expansion for Exchange in Solids and Surfaces". en. In: *Physical Review Letters* 100.13 (Apr. 2008), p. 136406. ISSN: 0031-9007, 1079-7114. DOI: 10.1103/PhysRevLett.100.136406.

[32] Koichi Eguchi, Takeo Tokiai, and Hiromichi Arai. "High pressure catalytic hydration of olefins over various proton-exchanged zeolites". In: *Applied Catalysis* 34 (1987), pp. 275–287. ISSN: 0166-9834. DOI: https://doi.org/10.1016/S0166-9834(00)82462-8. URL: http://www.sciencedirect.com/science/article/pii/S0166983400824628.

A

Appendix

A.1 Computational resources

The DFT calculations done throughout this thesis were performed on the various clusters provided by Swedish National Infrastructure for Computing (SNIC).